CONDUCTION AND BREAKDOWN IN DIELECTRIC LIQUIDS

For greater efficiencies in ac and dc power generation and transmission, and for larger energies in such pulsed power applications as lasers, inertial confinement fusion, charged particle beam devices, and directed energy devices, it is necessary to operate at the highest voltage levels with minimum volume. These technologies are thus often limited by the conduction properties and electrical breakdown strength of liquid insulation.

The study of electrical insulation and dielectric phenomena is often empirical, with most measurements made at electrical terminals of voltage and current, thus providing no information on the electric field distribution throughout the volume between electrodes. These terminal measurements cannot distinguish among a wide range of models of conduction, charge injection, prebreakdown and breakdown behavior. The electric field distributions cannot be calculated from knowledge of system geometries alone because of space charge and surface charge effects including electrohydrodynamic convection. This volume and surface charge are often due to flow electrification, injection from electrodes and/or interfacial space-charge layers, or to dielectric ionization; also they depend on the electric and flow velocity fields, which, in turn, through Gauss's and Coulomb's laws, depend self-consistently on the charge and Coulombic force distributions.

OVERVIEW OF LIQUID DIELECTRICS

Properties and Applications

In practical applications liquids are often better electrical insulators than solids and gases. Their high density from Paschen's law indicates a higher breakdown strength than gas. Liquids fill the space to be insulated and by thermal conduction and convection, help dissipate thermal losses. They are often self-healing after a spark discharge as the debris is dispersed or carried away by a flow. They also increase the rate of heat transfer by their high thermal conductivity and by convection (1–5). Transformer oil is about 20–30 times more effective than air in removing the heat generated in the windings and magnetic core of a transformer. A solid offers the advantage of mechanical strength but often has voids that are not self-healing after electrical breakdown because the insulation is punctured leaving a carbonized discharge channel that is conducting.

Most insulating liquids used in transformers, cables, capacitors, switches, and circuit breakers are complex mixtures of paraffinic, napthenic and aromatic hydrocarbons. The paraffinic base is characterized by the chemical formula $C_{2n}H_{2n+2}$, the napthenes by $C_{2n}H_{2n}$, and the aromatics by C_nH_n. Napthenic oils are generally preferred because they are less viscous and have good gas-absorbing properties.

These oils have relative dielectric constants of about 2, a dissipation factor of about 0.001 at 60 Hz, working electrical breakdown strength of about 120 kV/cm, and a resistivity greater than $10^{10}\ \Omega \cdot m$. They are highly flammable, but the hazard from fire is minimal when operating at a temperature far below the flashpoint.

In transformers, the oil serves the dual function of high voltage insulation and cooling with oil flow. Analysis of the insulating oil in an operating transformer provides information on the robustness of the system. This monitoring has become more important in recent years due to the trend toward higher voltages and smaller size, thereby increasing the design stress. This has lead to the development of on-line hydrocarbon gas monitors, indicators of the degradation of cellulosic insulation, computerized methods to predict temperatures throughout transformer windings by calculating precise oil flow and heat flux, and development of microprocessor-based transformer monitors to improve control, avoid failures, and to extend the lifetime of in-service transformers.

Moisture is the most common cause of deterioration, either as tiny droplets mixed with the oil as an emulsion or as a pool at the bottom of the transformer when the droplets coalesce to form larger drops that sink to the bottom. A slower but more damaging deterioration is the formation of acids and sludge, caused by oxidation. Fault conditions such as overheating (hot spots), partial discharges (corona), and continuous arcing lead to accumulation of combustible gases and to chemical degradation of the oil, resulting in changes in the molecular weight distribution.

In the recent past, mineral oil flammability was reduced by adding polychlorinated biphenyls (PCB). However, later research has shown that the nonbiodegradability of PCBs is a health hazard so that current standards do not allow the use of PCB oil. This has resulted in a search for new natural or synthetic oils that are biologically and environmentally safe, yet still have high electric strength, low dielectric dissipation, good chemical stability, low volatility and high flashpoint, good arc-quenching properties, and are nonflammable, nontoxic, and inexpensive. Silicone oil is an expensive candidate for replacement of PCB-contaminated oil.

In recent years, utilities and other users of liquid filled transformers have also shown an interest in biodegradable insulating fluids as alternatives to currently available dielectric fluids (6). This interest is based on the low biodegradability levels of currently available dielectric fluids and the environmental concerns that could result from spills of these fluids. Several vegetable oils have been tested for possible use in transformers. It was found that naturally stable oils are preferable candidates, but further stabilization is needed for use in transformers.

Since the banning of PCBs, new fluids have also been developed for use in capacitors (2). The major function of these capacitor fluids is the prevention of partial discharges. High discharge inception voltage fluids which inhibit electron injection into the fluid include paraffinic mineral oils and polydimethyl siloxanes. Both aliphatic and aromatic liquids have high discharge inception voltages but aromatic liquids also have slightly lower discharge extinction voltages. Thus low molecular derivatives of benzene are typically used as capacitor liquids because once discharges start, the voltage has only to be reduced by a small amount to extinguish the discharges. Typical capacitor liquids are isopropylbiphenyl, propylbiphenyl, methylated diphenylethane, phenylxylylethane, benzyl neocaprate, camylphenylethane, ditolyether, dioctylphthalate, phosphate esters, and mono/dibenzyltoluene.

Organic esters with high dielectric constant, such as ethylene glycol ($\epsilon_r \approx 40$) as well as castor oil ($\epsilon_r \approx 3.7$), dibutyl sebacate ($\epsilon_r \approx 4.4$), butyl stearate ($\epsilon_r \approx 3.3$), and silicate esters ($\epsilon_r \approx 2.6$) have been used in cables and high-frequency capacitors, especially because they also generally have low losses at high frequencies.

Synthetic hydrocarbons such as the polybutenes, polyalphaolefins, alkyl-substituted aromatics, and halogenated aliphatic hydrocarbons have found use as electrical insulators. Polybutenes, polyalphaolefins, and alkyl-substituted aromatic compounds are gas absorbing under electrical stress or partial discharge leading to oxidation that forms organic acids. They thus require oxidation inhibitors to have acceptable oxidation stability. Polybutene performs well in dc systems while polyalphaolefins have found use as a PCB replacement fluid.

Stable hydrogenated hydrocarbons have all hydrogens replaced by halogens. The most stable are fluorocarbons, which have been used as refrigerants but have also been used in vapor-cooled transformers.

To decrease power dissipation in transformers, oil and pressboard insulation are dried to remove moisture. However, as drying processes have been improved, a new problem has arisen—flow-induced electrification. Here, the mobile part of the electrical double layer that forms at the interface of dissimilar materials is swept away by oil flow, leaving behind the countercharge on the interface. The net accumulation of charge on highly insulating or isolated surfaces leads to strong electric fields and ultimately to spark discharges that can cause a transformer to fail.

Electrical Breakdown Mechanisms

Electrical breakdown in liquids is thought to be due primarily to:

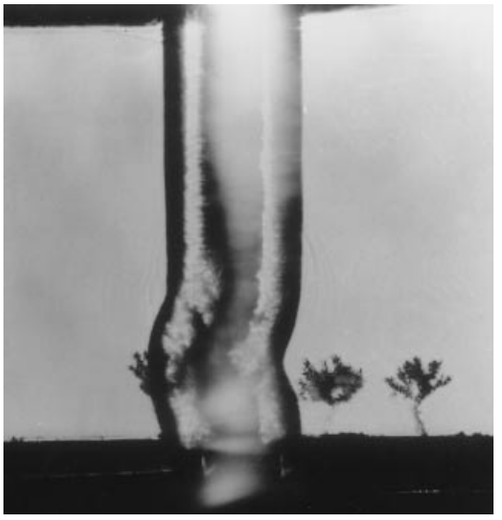

Figure 1. Parallel-plate electrodes with a hydrocarbon dielectric (toluene) stressed by a 250 kV pulse show electrical trees emanating from the cathode, one of which led to the breakdown streamer that short-circuits the 5 mm gap. The photograph was taken about 200 ns after electrical breakdown.

1. Electronic avalanches as in gases
2. Bubbles that form near surface irregularities on electrodes, which concentrate the electric field and cause Joule heating that boils the liquids to form bubbles; once a gas region is formed, avalanche theory describes the breakdown phenomena in the gaseous bubble. Figure 1 shows a hydrocarbon liquid stressed by a high-voltage pulse. The electron avalanches within the vapor region grow into tree-like structures at the cathode that initiate the breakdown streamer shown.
3. Suspended particles that form chains along the electric field to partially short circuit the gap

An understanding of electrical breakdown in gases can also be applied to a bubble breakdown model in liquids. The fundamental phenomenon is described by the Paschen curve of gas breakdown voltage of Fig. 2 for a gap d (7–9). When the

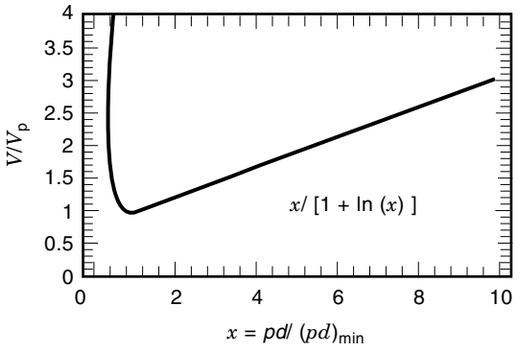

Figure 2. The universal Paschen curve describes the voltage breakdown strength in gases as a function of the pressure-gap (pd) product. The nondimensional function given in the plot with voltage and pressure-gap product normalized to the Paschen minimum voltage V_p and $(pd)_{min}$ approximates measured curves (9).

applied electric field in a gas exceeds V_p/d, the onset of corona results in light, UV radiation, audible noise, radio-frequency interference, nitric acid in the presence of moisture and air, heat generation and power loss, and mechanical erosion of surfaces by ion impacts. Corona partial discharges are localized ionizations of gas forming a plasma of electrons, ions, excited molecules and free radicals. These form chemically reactive species that often degrade nearby liquid and solid interfaces. Corona is often pulsating, as the buildup of charge near the electrode causes a decrease in the electric field below that necessary to sustain charge emission or dielectric ionization. Corona can be reduced by rounding sharp edges to lower the local electric field. Above the Paschen minimum, an increasing pressure reduces the mean free path between collisions and higher voltages are necessary for ionization, thereby preventing corona. For typical gases the Paschen minimum voltage V_p varies from 137–457 V with a pressure-distance $(pd)_{min}$ product at the Paschen minimum varying over the range of 0.4–5.3 Pa-m.

With high over-voltages above the Paschen curve in a uniform electric field gap, avalanches in gaseous regions in a liquid grow into irregular filamentary luminous branches known as streamers, as shown in Fig. 1. According to streamer theory, ionization from an avalanche increases the conductivity and the emitted light increases photoionization of gas molecules ahead of the streamer. This causes a space-charge distribution that increases the electric field at the tip of the streamer, thereby continuing the avalanche growth.

LIQUID INSULATION SYSTEMS

Physical Properties

From the current state of knowledge of oil aging and degradation, the power industry has developed measurement procedures, interpretation, and corrective actions from the monitoring of electrical, physical, chemical, and thermal properties of oils (10).

The dielectric breakdown strength is important at 50/60 Hz power frequency as a measure of the ability of the liquid to withstand electric stress at operating and test voltages without failure. Low values indicate the presence of contaminants such as water, dirt, conducting particles or gas evolution. Impulse testing is used to simulate transient voltage stresses arising from such causes as lightning strokes and high-voltage switching.

High resistivity reflects the low content of free ions and ion-forming particles, and normally indicates a low concentration of conductive contaminants. Resistivity of less than 15 MΩ-cm generally indicates problems.

Oil becomes darker with age because of the formation of acids, resins, and sludge from insulating materials in the transformer. The color should not progress beyond a light brown, remaining clear and free from turbidity or cloudiness. Black coloring or floating carbon particles indicates severe arcing.

The flash and fire points indicate the flammability of an oil. The flash point is the temperature at which vapors above the oil surface first ignite when a small test flame is passed across the surface. The fire point is the temperature at which the oil first ignites and burns for at least 5 s when a small test flame is passed across the surface.

Interfacial tension is a reliable indication of the presence of hydrophilic compounds, which are soluble polar contaminant products of oxidation. A high interfacial tension indicates the absence of undesirable polar contaminants. Interfacial tension is frequently measured in service-aged oils as an indication of the degree of deterioration.

Pour point is the lowest temperature at which the oil is observed to flow when cooled without seriously limiting the degree of circulation.

Changes in refractive index with service indicate changes in composition or the degree of contamination.

Viscosity influences heat transfer properties and consequently the temperature rise. At low temperatures, the higher viscosity influences the speed of moving parts such as load tap-changer mechanisms and pumps. Viscosity controls such mineral insulating oil processing conditions as dehydration, degasification and filtration, and oil-impregnation rates. Viscosity affects pressure drop, oil flow, and cooling rates in circulating oil systems.

Acidity in used insulating oils can be compared to new oil in detecting contaminants or chemical changes, and can be used as a measure for determining when an oil should be replaced to prevent further decomposition and consequent sludging. For a power transformer 500 kVA and larger operating at 60°C maximum rise, the transformer oil should reach the critical acid number of 0.25 mg/KOH/g in about 15 years.

Gas analysis measures oil decomposition due to temperature and spark discharges and other aging mechanisms by the gases dissolved in electrical insulating oil, including the following: hydrogen (H_2); nitrogen (N_2); carbon monoxide (CO); carbon dioxide (CO_2); oxygen (O_2); methane (CH_4); ethane (C_2H_6); ethylene (C_2H_4); acetylene (C_2H_2); propane (C_3H_8); and propylene (C_3H_6).

New electrical insulating oil may contain phenolic oxidation inhibitors, 2,6-di-*tert*-butyl-*p*-cresol (DBPC) and 2,6-di-*tert*-butylphenol, which reduces oil color, acidity, and sludge in operating transformers. Minimizing the development of oil sludge and acidity resulting from oxidation during storage, processing, and long service life reduces electrical conduction and metal corrosion; it also increases insulation system life, electrical breakdown strength and heat transfer. Open breathing transformers have faster oxidation deterioration than sealed transformers. The rate of oxidation generally doubles with each 10°C increase.

Water in insulating liquids is generally measured by the Karl Fischer method, usually in the range of 0 to 75 ppm. The method is based essentially on the reduction of iodine by sulfur dioxide in the presence of water. A low water content is necessary to achieve adequate electric strength, low dielectric losses, maximize insulation life, and minimize metal corrosion. A normal power transformer will have a water content under 2% in the paper and 10 to 20 ppm in the oil.

Analysis of Gas in Transformer Oils

A study of gas formation in transformer oil stressed by high fields frequently gives an early indication of abnormal behavior in a transformer and can allow corrective action before the equipment suffers greater damage (11). Improvements in available instrumentation allow utilities to adopt oil-analysis programs as failure-prevention programs rather than just failure-analysis programs. The distribution of gases is related to the type of fault, and the rate of gas formation is indicative of the severity of the fault.

Fault gases are generally due to corona or partial discharge, pyrolysis or thermal heating, and arcing. The hydrocarbon gases methane (CH_4), ethane (C_2H_6), ethylene (C_2H_4), and acetylene (C_2H_2) are produced by mineral oil decomposition. Carbon dioxide (CO_2) and carbon monoxide (CO) arise from thermal decomposition of the cellulosic insulating material. Hydrogen (H_2) is a component of both cellulosic material and any water present in the oil. Oxygen (O_2) and nitrogen (N_2) are not considered fault gases, but are usually present.

Arcing causes large amounts of hydrogen and acetylene to be produced, with minor quantities of methane and ethylene. Carbon dioxide and carbon monoxide may also be formed if the fault involves cellulose; the oil may be carbonized.

Low-energy electrical discharges from corona produce hydrogen and methane, with small quantities of ethane and ethylene. Comparable amounts of carbon monoxide and dioxide may result from discharges in cellulose.

Decomposition products from overheated oil include ethylene and methane, together with smaller quantities of hydrogen and ethane. Traces of acetylene may be formed if the fault is severe or involves electrical contacts.

Large amounts of carbon dioxide and carbon monoxide are evolved from overheated cellulose. Hydrocarbon gases, such as methane and ethylene, will be formed if the fault involves an oil-impregnated structure.

All these gases are dissolved in the oil as well as in the gas blanket above the oil. Due to differences in solubilities of these gases in the oil, their distribution in the oil and gas blanket will differ. Equal quantities of hydrogen and acetylene in the gas blanket will result in concentrations in the oil that differ by almost two orders of magnitude because hydrogen is least soluble in oil while acetylene is most soluble in the oil.

The energy released by any fault, including heat, fragments the oil into smaller hydrocarbon chains and hydrogen. Corona leads to large amounts of hydrogen; sparking gives rise to methane and ethane; severe local heating causes the formation of ethylene; and arcing forms acetylene. These are the key gases for each fault type, but other gases can also be formed. Faults near cellulosic materials give rise to carbon dioxide and carbon monoxide, with the ratio of carbon monoxide to carbon dioxide increasing as the severity of the faults increases.

The most widely used measurement method determines the total combustible gases present above the oil. It is rapid and can be continuously monitored, but it does not determine which fault gases are present and therefore cannot indicate either the type or severity of a fault.

Normal oil aging has up to 500 ppm fault gases. Decomposition may be in excess of normal aging with gas levels of 500 to 2500 ppm, while severe problems are developing for gas levels above 2500 ppm.

A rate of increase of combustible gas generation of 100 ppm or more for a 24-h period on a continuing basis, with a relatively constant load, indicates a deteriorating condition and requires an assessment of continued operation, especially if acetylene is in excess of 20 ppm.

Dissolved gas analysis (DGA) takes a sample of oil; the dissolved gases are extracted and then separated, identified,

and quantitatively determined using a gas chromatograph to detect fault gases at the earliest point in time and can ascertain the type and severity of the fault.

Because dissolved hydrogen in oil is of the same order of concentration as the other fault gases, hydrogen monitors using hydrogen diffusion through a Teflon or polyimide membrane have been developed for cheaper and easier measurements that allow continuous monitoring.

Faults of thermal or electrical origin can be differentiated by comparing pairs of gases with approximately equal solubilities and diffusion coefficients. Thus, an increase in the ratio of ethylene to acetylene above unity indicates an electrical fault while the ratio of methane to hydrogen exceeding 0.1 suggests a thermal fault and less than 0.1 suggests a corona discharge.

A thermodynamic assessment of the formation of the simple decomposition of gaseous hydrocarbons based on equilibrium pressures at various temperatures suggests that the proportion of each gaseous hydrocarbon in comparison with each of the other hydrocarbon gases varies with the temperature of decomposition. This leads to the assumption that the rate of evolution of any particular gaseous hydrocarbon varies with temperature, and that at a particular temperature there would be a maximum rate of evolution where each gas attains the maximum rate at a different temperature. These thermodynamic equilibria suggest that with increasing temperature, the maxima would be in turn methane, ethane, ethylene, and acetylene.

Flow Electrification

Static electrification due to liquid dielectric flow has been found to be the cause of about two dozen field failures worldwide of large forced-oil-cooled power transformers (12). Problems stem from the entrainment of diffuse double-layer charge at interfaces into circulating liquid. The accumulation of this charge in the volume, or the deposition of this charge on insulating or isolated surfaces, causes the electric potential to rise in the same fashion as voltage build-up in a Van de Graaff generator. The potential builds up until the rate of charge accumulation equals the rate of charge leakage, or until spark discharges occur. Electrification effects are initiated by fluid flow, whether or not the equipment is energized. Energization generally augments the electrification effect.

Understanding of electrification requires the coupling of the laws of electromagnetism, fluid mechanics, heat, and electrochemistry to describe the generation, transport, accumulation, and leakage of charge, and to relate how these factors are affected by temperature, moisture, flow rate and turbulence, contaminants, additives, and surface active agents, wall surface condition, energization, and flow configuration. What makes understanding difficult is that there is a lack of common factors in failures. Identical side-by-side transformers have different failure experiences. Trace differences in material properties and impurities that are not easily controlled, apparently have a strong effect on flow electrification.

Charge separation at interfaces between moving fluid and boundaries with the accumulation of charge on insulators or isolated conductors can lead to high field strengths and electrical discharges. Electrification has been a problem in the past in the flow of petroleum liquids in pipes and through filters and in charge accumulation in storage tanks (13). Electrostatic spark discharges in the vapor of these combustible fluids has resulted in explosions and fires. To avoid these hazards, all metallic surfaces are grounded to prevent the electric potential from rising above the breakdown strength of the surrounding medium; the flow rate is reduced to decrease the rate of charging, and antistatic additives are added to the fluid to raise its conductivity so that any accumulation of net charge relaxes with time constant given by the dielectric relaxation time. These measures have essentially eliminated flow electrification problems in the transport, filtering, filling, and storage operations of petroleum products.

The fixes used in the petroleum industry cannot always be applied to electric power equipment. Grounded conductors are not possible in high-field regions, while a decrease in the flow speed of coolant may be a major limitation in the power rating. Raising the conductivity of the insulating fluid with antistatic additives may also increase the losses, making the device less efficient.

The predominant charge separation process occurs in the insulation ducts, which are made up of insulation paper wound coils and pressboard washers. These insulation parts acquire a negative charge while the flowing oil is positively charged. Negative charge accumulation occurs in the lower part of the insulation structure while the upper tank where the oil exits the duct builds up a positive charge. Inspection of failures shows that flashovers generally occur between a high-voltage winding and a low-voltage lead spanning several inches of oil, normally considered adequate for safe operation. Severe tracking occurs in the lower part of the pressboard insulation structure, as illustrated in Fig. 3. In all cases of catastrophic failure, the units were energized with pumps

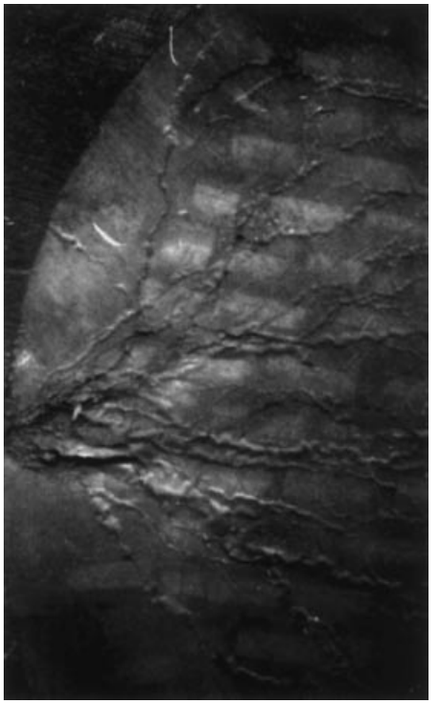

Figure 3. Tracking surface discharges for a failed transformer at the bottom of the high to low pancake washer where the entering oil velocity is high.

operating. Less severe cases of electrification have been observed with unenergized transformers but with pumps operating.

The flow electrification problem has often arisen when a transformer that has been out of service is being recommissioned. As the transformer heats up, moisture is driven out of the pressboard insulation into the oil. This moisture first comes from the area near the pressboard interface, leaving a very dry interface that is also highly insulating. None of the accumulating surface charge has leakage; thus the surface-charge density can increase until surface-tracking discharges occur. These sparks cause gas formation, which can rise into the high-electric field region causing a high-energy discharge that causes transformer failure. Typical surface-tracking discharges are shown in Fig. 3. If failure does not occur during the early times of the recommissioning process, then moisture deeper in the pressboard diffuses to the surface, reaching equilibrium with the oil moisture. The moisture-diffusion time can easily be a few weeks, but once there is no longer an insulating interfacial dry zone, there is a leakage path for interfacial surface charge so that the surface-charge density cannot cause electric field strengths beyond the breakdown strength of oil and pressboard. Thus, if this scenario is correct, once the transformer is in moisture equilibrium, the flow electrification hazard is minimized.

Japanese transformer manufacturers believe that the problem has been solved by using the nonionizable antistatic additive benzotriazole (BTA), but the long-term effects of BTA as it leaves the oil volume onto pressboard surfaces and tank walls is not well understood (14). Even without additive, the electrification problem can be minimized by not turning on cooling pumps when the transformer is lightly loaded. The most dangerous period seems to be when the transformer has been out of service and is then being recommissioned. The best method for recommissioning to avoid electrification-induced discharges is to increase load slowly so that the transformer can rise in temperature slowly enough to allow the oil and pressboard to be near moisture equilibrium. In this way, the formation of highly insulating interfacial dry zones where charge can accumulate to values sufficiently high to cause spark discharges and subsequent gas formation is avoided.

Pulsed Power Technology

For inertial confinement fusion and directed energy devices, high peak power at the terawatt level is needed for short times of the order of 100 ns. Pulsed power technology collects and stores electric energy at a low input power (~1 kW) for a long time (~1 s) and then delivers this 1 kJ energy in a much shorter time (~100 ns) at a much higher power level (10 GW) for a power gain of 10^7 (15).

Figure 4 illustrates a representative pulsed power machine called a Particle Beam Fusion Accelerator (PBFA) used in inertial confinement fusion experiments. The complete machine consisted of 36 such modules with ratings of 2 MV, 15 MA delivered for 35 ns, with 30 TW peak power and 1 MJ energy. The Marx generator capacitor bank that applies a high-voltage pulse to the pulse-forming line is generally transformer-oil insulated. Highly purified water is used as the dielectric in pulse-forming lines of most pulsed power machines because its high relative dielectric constant (~80) and high resistivity (>18 MΩ-cm) allow short and efficient low-impedance high-voltage lines for pulse durations less than 100 μs. Water/ethylene glycol mixtures have higher resistivity and allow low-temperature operation with negligible loss for longer millisecond time-scales. Thus rotating machinery, rather than the usual Marx generator, can be used as the primary energy store.

However, research has shown that charge injection into water can play an important role in determining the limits of performance of the dielectric. Injection of space charge from the electrodes into the water affects the charging and dis-

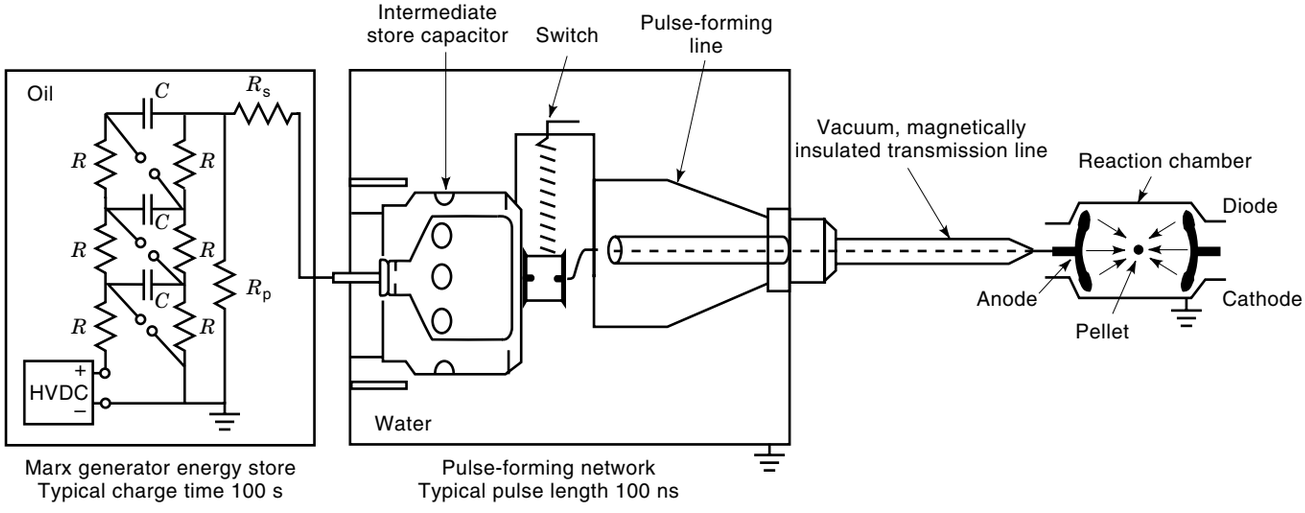

Figure 4. A representative pulsed power machine used for inertial-confinement fusion experiments consists of a slowly charged Marx capacitor bank under insulating oil as primary energy storage, a water dielectric capacitor as intermediate energy storage, a switched pulse-forming line that compresses the voltage in time, and a magnetically and vacuum-insulated transmission line that delivers the power pulse to a vacuum diode to produce energetic electrons or light ions, which are then accelerated and focused by electric and magnetic fields onto a target, typically a deuterium–tritium pellet.

charging circuit characteristics and introduces another time constant—the time of flight for injected charge to migrate between electrodes. High-voltage open-circuit decay curves of a 20% water/80% ethylene glycol mixture by weight have a dielectric relaxation time that depends on electrode spacing and that decreases with increasing initial voltage at room temperature (16). The nominal room-temperature low-voltage dielectric relaxation time is ~1.4 ms, while at −10°C the low-voltage dielectric relaxation time is ~25 ms, but where the open-circuit decay curve has an initial negative curvature with respect to time. This is in contrast to the expected exponential decay, which always has a positive curvature and with dielectric relaxation time that is independent of electrode geometry and voltage. This anomalous behavior is due to injected charge that increases the effective ohmic conductivity σ to $\sigma + \rho_+\mu_+ - \rho_-\mu_-$, where ρ_+ and ρ_- are the time- and space-dependent net charge densities of positive and negative charge carriers with respective mobilities μ_+ and μ_-.

CHARGE INJECTION AND CONDUCTION

Linear Lossy Dielectrics

Governing Equations of Ohmic Conduction. In most electrical insulation applications the frequency or time rates of change of electric field are sufficiently slow that Maxwell's equations are well approximated in their electroquasi-static limit. Then electrically insulating materials are essentially capacitive with the material characterized by its dielectric permittivity ϵ. Maxwell's equations can then be written as

$$\nabla \times \mathbf{E} = 0 \Rightarrow \mathbf{E} = -\nabla\Phi \tag{1}$$

$$\nabla \cdot \mathbf{E} = \rho/\epsilon \Rightarrow \nabla^2\Phi = -\rho/\epsilon \tag{2}$$

$$\nabla \cdot \mathbf{J} + \frac{\partial \rho}{\partial t} = 0 \tag{3}$$

where, for simplicity, we take ϵ to be a constant in the region of interest. The irrotational electric field $\mathbf{E}$ in Eq. (1) derives from Faraday's law with negligible magnetic field, which allows the definition of the electric scalar potential Φ. In Eq. (2), Gauss' law relates the electric field to the net source volume charge density $\rho = \rho_+ + \rho_-$. Together with Eq. (1), Eq. (2) shows that the potential Φ obeys Poisson's equation. Conservation of charge in Eq. (3) relates the current density $\mathbf{J}$ to the time rate of change of charge density.

For electrical insulation applications it is usually desired that the current density $\mathbf{J}$ be as small as possible. Many materials are accurately described by an ohmic constitutive law where σ is the ohmic conductivity

$$\mathbf{J} = \sigma\mathbf{E} \Rightarrow v = iR \tag{4}$$

which is the field form of the familiar circuit Ohm's law proportionality relating voltage v to current i via resistance R.

A homogeneous lossy dielectric between a pair of electrodes at voltage difference v has a circuit model of resistance R in parallel with capacitance C such that

$$RC = \epsilon/\sigma \tag{5}$$

where the RC product is independent of voltage, electrode shape, area, or spacing.

Transient and Convective Charge Relaxation. Substituting Ohm's law of Eq. (4) into Eq. (3) for constant conductivity σ yields

$$\sigma\nabla \cdot \mathbf{E} + \frac{\partial \rho}{\partial t} = 0 \Rightarrow \frac{\partial \rho}{\partial t} + \frac{\sigma}{\epsilon}\rho = 0 \tag{6}$$

where the right-hand equation eliminates $\nabla \cdot \mathbf{E}$ using Eq. (2). The solution to Eq. (6) is

$$\rho(x, y, z, t) = \rho(x, y, z, t = 0)e^{-t/\tau} \tag{7}$$

where $\tau = \epsilon/\sigma$ is called the dielectric relaxation time and equals from Eq. (5) the circuit RC time constant. This solution shows that if any region of space has an initial volume charge distribution $\rho(x,y,z,t = 0)$, it will decay exponentially with time constant τ. If an ohmic region has no initial volume charge so that $\rho(x,y,z,t = 0) = 0$, then the volume-charge density remains zero in that region thereafter.

In charged liquids moving with velocity $\mathbf{U}$, there is a convection current $\rho\mathbf{U}$ in addition to a conduction current. For a convecting charged ohmic material, Eq. (4) becomes

$$\mathbf{J} = \sigma\mathbf{E} + \rho\mathbf{U} \tag{8}$$

and by substitution into Eq. (3), Eq. (6) is generalized to

$$\frac{\partial \rho}{\partial t} + \nabla \cdot (\rho\mathbf{U}) + \rho/\tau = 0; \tau = \epsilon/\sigma \tag{9}$$

As a special case, consider the dc steady state of a liquid moving at constant x directed velocity $\mathbf{U} = U\mathbf{i}_x$, through a high-voltage stressed screen at $x = 0$ with microscopic asperities that inject volume charge. For one-dimensional analysis, the dc steady-state form of Eq. (9) with U constant is

$$U\frac{\partial \rho}{\partial x} + \rho/\tau = 0 \tag{10}$$

If the charge-injecting screen maintains a constant charge density $\rho(x = 0) = \rho_0$, the solution to Eq. (10) is

$$\rho = \rho_0 e^{-\sigma x/\epsilon U} \tag{11}$$

We see that the charge density is convected over a relaxation length scale of order $\epsilon U/\sigma = U\tau$.

Interfacial Charge

Step Transient. Surface charge can accumulate on the interface between two dissimilar lossy dielectric materials. This is illustrated for the series lossy capacitor shown in Fig. 5 which is modeled by a pair of parallel RC circuits connected in series. We consider a step voltage applied at $t = 0$ to an initially unexcited system. Neglecting end effects, the electric field can only be in the x direction and at best vary with that coordinate. In the absence of any volume charge ($\rho = 0$), Eq. (2) for the electric field requires $dE_x/dx = 0$ so that the electric field in each region E_1 and E_2 is uniform in space within each lossy dielectric but can vary with time.

The interfacial form of Eq. (3) gives the required conservation of charge boundary condition at the interface as

$$J_2 - J_1 + \frac{\partial \sigma_s}{\partial t} = 0; \sigma_s = \epsilon_2 E_2 - \epsilon_1 E_1 \tag{12}$$

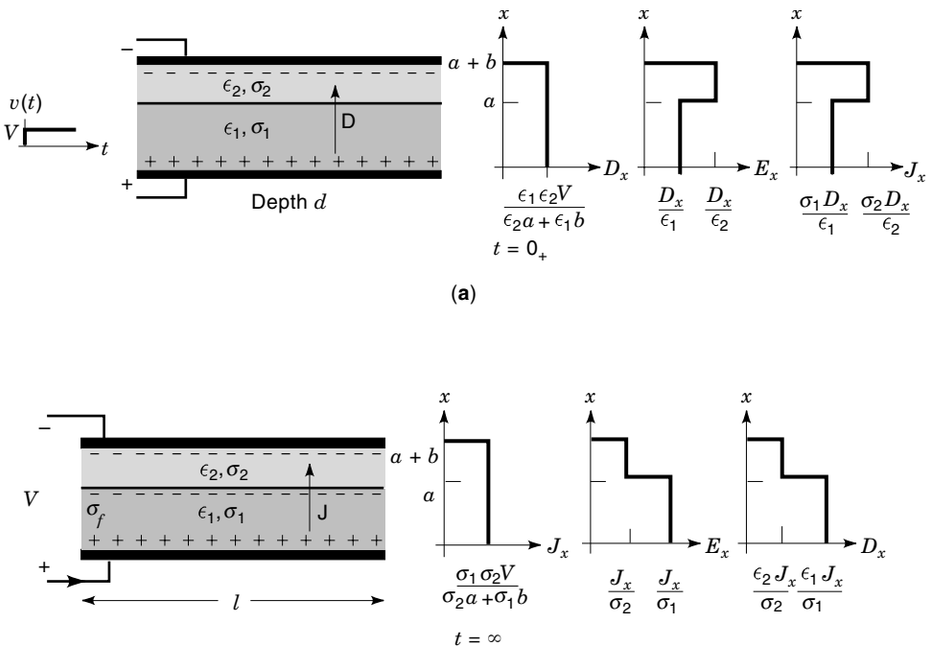

Figure 5. Two different lossy dielectric materials in series between parallel plate electrodes of width l and depth d have permittivities and ohmic conductivities that change abruptly across the interface; (a) at $t = 0_+$, right after a step voltage is applied, the interface is uncharged so that the displacement field $D = \epsilon_1 E_2 = \epsilon_2 E_2$ is continuous with the solution the same as that for two lossless dielectrics in series; (b) as the current is discontinuous across the boundary between the materials, the interface will charge up. In the dc steady state, the current density $J = \sigma_1 E_1 = \sigma_2 E_2$ is continuous; (c) each region is circuit equivalent to a resistor and capacitor in parallel.

where σ_s is the interfacial surface-charge density which equals the difference in perpendicular displacement fields ($\mathbf{D} = \epsilon\mathbf{E}$) across the interface.

At $t = 0_-$, the interfacial surface-charge density is zero and remains continuous at $t = 0_+$ so that $D = \epsilon_1 E_1 = \epsilon_2 E_2$, while in the dc steady state as $t \to \infty$, Eq. (12) requires that the current density $J = \sigma_1 E_1 = \sigma_2 E_2$ be continuous across the interface.

The solutions for the electric fields in each region are then

$$E_1 = \frac{\sigma_2 v}{\sigma_2 a + \sigma_1 b}(1 - e^{-t/\tau}) + \frac{\epsilon_2 v}{\epsilon_2 a + \epsilon_1 b} e^{-t/\tau}$$
$$E_2 = \frac{\sigma_1 v}{\sigma_2 a + \sigma_1 b}(1 - e^{-t/\tau}) + \frac{\epsilon_1 v}{\epsilon_2 a + \epsilon_1 b} e^{-t/\tau} \tag{13}$$

where the time constant

$$\tau = \frac{\epsilon_1 b + \epsilon_2 a}{\sigma_1 b + \sigma_2 a} \tag{14}$$

is a thickness weighted average of relaxation times in each material. The interfacial surface charge density is

$$\sigma_s = \epsilon_2 E_2 - \epsilon_1 E_1 = \frac{(\epsilon_2 \sigma_1 - \epsilon_1 \sigma_2) v}{\sigma_2 a + \sigma_1 b}(1 - e^{-t/\tau}) \tag{15}$$

which is zero at $t = 0$ and increases to a steady-state value with polarity proportional to $(\epsilon_2/\sigma_2 - \epsilon_1/\sigma_1)$.

Sinusoidal Steady State. If rather than a step voltage the applied voltage is sinusoidal, the electric fields in each region will also vary sinusoidally with time

$$v(t) = \mathrm{Re}\{\hat{v} e^{j\omega t}\} \Rightarrow E_1(t) = \mathrm{Re}\{\hat{E}_1 e^{j\omega t}\}, E_2(t) = \mathrm{Re}\{\hat{E}_2 e^{j\omega t}\} \tag{16}$$

In Eq. (16) it is convenient to use complex notation where the careted symbols represent complex amplitudes. Then Eq. (12) requires that the sum of conduction and displacement current

densities be continuous across the interface

$$(\sigma_2 + j\omega\epsilon_2)\hat{E}_2 = (\sigma_1 + j\omega\epsilon_1)\hat{E}_1 \tag{17}$$

The electric field complex amplitudes are then related as

$$\frac{\hat{E}_2}{(j\omega\epsilon_1 + \sigma_1)} = \frac{\hat{E}_1}{(j\omega\epsilon_2 + \sigma_2)} = \frac{\hat{v}}{[b(\sigma_1 + j\omega\epsilon_1) + a(\sigma_2 + j\omega\epsilon_2)]} \tag{18}$$

and the interfacial surface charge density complex amplitude is

$$\begin{aligned}\hat{\sigma}_s &= \epsilon_2\hat{E}_2 - \epsilon_1\hat{E}_1 \\ &= \frac{(\epsilon_2\sigma_1 - \epsilon_1\sigma_2)\hat{v}}{[b(\sigma_1 + j\omega\epsilon_1) + a(\sigma_2 + j\omega\epsilon_2)]}\end{aligned} \tag{19}$$

Electrical Double Layer

Governing Equations of Drift-Diffusion Conduction. With slight fluid ionization, either by normal dissociation, trace impurities or by use of additives, insulating liquids carry positive and negative ions of charge magnitude q. These ions try to neutralize each other in the bulk, but at boundaries there is a preferential adsorption of one species with the opposite carrier diffusely distributed over a thin boundary region called the electrical double layer. The degree of net charge and the depth to which it penetrates into the liquid volume are related by the balance of ion diffusion, migration, and convection. In stationary equilibrium, diffusion due to concentration gradients is balanced by the electric field induced by the separated charges.

The current densities $\mathbf{J}_+$, $\mathbf{J}_-$, with positive and negative charge carriers with volume densities ρ_+, ρ_-, respective mobilities μ_+, μ_-, and diffusion coefficients D_+, D_-, are

$$\begin{aligned}\mathbf{J}_+ &= \rho_+\mu_+\mathbf{E} - D_+\nabla\rho_+ \\ \mathbf{J}_- &= -\rho_-\mu_-\mathbf{E} - D_-\nabla\rho_-\end{aligned} \tag{20}$$

where Einstein's relation relates these parameters to the thermal voltage

$$\frac{D_+}{\mu_+} = \frac{D_-}{\mu_-} = \frac{kT}{q} \tag{21}$$

where $k = 1.38 \times 10{-}^{23}$ J/K is Boltzmann's constant and T is the temperature in degrees Kelvin. In equilibrium, the net current of each carrier is zero, $\mathbf{J}_+ = \mathbf{J}_- = 0$, so that Eqs. (20) and (21) require that the charge densities obey Boltzmann distributions with the electric field $\mathbf{E}$ related to the potential distribution Φ as $\mathbf{E} = -\nabla\Phi$

$$\begin{aligned}\rho_+ &= \rho_0 e^{-q\Phi/kT} \\ \rho_- &= -\rho_0 e^{q\Phi/kT}\end{aligned} \tag{22}$$

where $\pm\rho_0$ is the equilibrium charge density of each carrier when the potential is zero ($\Phi = 0$).

To find the spatial dependence of net charge density $\rho = \rho_+ + \rho_-$ and potential Φ in the dielectric with permittivity ϵ, we use Eq. (22) in Poisson's equation

$$\nabla^2\Phi = -\left(\frac{\rho_+ + \rho_-}{\epsilon}\right) = \frac{\rho_0}{\epsilon}[e^{q\Phi/kT} - e^{-q\Phi/kT}] = \frac{2\rho_0}{\epsilon}\sinh\frac{q\Phi}{kT} \tag{23}$$

known as the Poisson–Boltzmann equation. A strict theory would require individual conservation equations for both carriers and neutral species, including finite rates of recombination and generation. However, in general, the local charge densities of each carrier are usually not far from their equilibrium values and a good approximation is that potentials are much less than the thermal voltage $q\Phi/kT \ll 1$. Then Eq. (23) can be linearized to

$$\nabla^2\Phi - \frac{\Phi}{\lambda^2} = 0;\ \lambda = \left[\frac{\epsilon kT}{2\rho_0 q}\right]^{1/2} = \left[\frac{\epsilon}{2\rho_0}\frac{D_\pm}{\mu_\pm}\right]^{1/2} \approx \left[\frac{\epsilon D}{\sigma}\right]^{1/2} \tag{24}$$

where λ is called the Debye length and indicates the length scale of noncharge neutrality. In the last equality we also relate the Debye length to the ohmic conductivity $\sigma = \rho_0(\mu_+ + \mu_-) \approx 2\rho_0\mu_\pm$ assuming $\mu_+ \approx \mu_-$ so that $D_+ \approx D_- = D$.

For the case of a charged sheet at potential ζ at $x = 0$, the potential, electric field, and net charge-density distributions for $x > 0$ are

$$\Phi = \zeta e^{-x/\lambda},\ E = -\frac{d\Phi}{dx} = \frac{\zeta}{\lambda}e^{-x/\lambda},\ \rho = \epsilon\frac{dE}{dx} = -\frac{\epsilon\zeta}{\lambda^2}e^{-x/\lambda} \tag{25}$$

where the wall volume charge density on the liquid side is related to the zeta potential as $\rho_w = \rho(x = 0) = -\epsilon\zeta/\lambda^2$.

In aqueous electrolytes, $\sigma \approx 10^{-1}$ S/m, $D \approx 10^{-10}$ m^2/s, and $\epsilon \approx 80\epsilon_0 \approx 7 \times 10^{-10}$ F/m, so that $\lambda \approx 8 \times 10^{-10}$ m is extremely small. A zeta potential of order of the thermal voltage at room temperature $\zeta \approx kT/q \approx 0.025$ V across this double layer results in a very large internal electric field $E \approx \zeta/\lambda \approx 3 \times 10^7$ V/m. Because of the large conductivity in aqueous electrolytes, externally applied fields cannot approach such magnitudes and thus hardly disturb the electrical double-layer equilibrium. Similarly, convection has a negligible effect as is seen by comparing the electrical relaxation time $\tau_e = \epsilon/\sigma \approx 84$ μs to a liquid transport time $\tau_t \approx L/U$, where L is a characteristic travel length of a fluid moving at a velocity U. For representative values of $L = 1$ cm and $U \approx 1$ m/s, $\tau_t \approx 0.01$ s is much greater than τ_e. The ratio of these times is called the electric Reynold's number $R_e = \tau_e/\tau_t = \epsilon U/\sigma L \approx 0.0084 \ll 1$. Because $R_e \ll 1$, the effect of convection in electrolytes on the charge distribution is small.

The mobility μ(m^2/V·s) of ions in highly insulating dielectric fluids is empirically related to the fluid viscosity η[N − s/m^2] by Walden's rule (17)

$$\mu \approx \frac{2 \times 10^{-11}}{\eta}\ (m^2/V \cdot s) \tag{26}$$

Transformer oil at 20°C has $\eta \approx 20$ cp $= 0.02$ N $=$ s/m^2 so that $\mu \approx 10^{-9}$ m^2/V·s). Then from Einstein's relation of Eq. (21), the molecular diffusion coefficient at 300°K is $D \approx 2.5 \times 10^{-11}$ m^2/s. For a typical transformer oil conductivity of $\sigma \approx 10^{-12}$ S/m and permittivity $2.2\epsilon_0 \approx 1.95 \times 10^{-11}$ F/m, the Debye length is $\lambda \approx 22$ μ. The internal electric field is then $E \approx (kT/q)/\lambda \approx 1.1$ kV/m.

With such low internal electric fields, reasonable externally applied fields are significant in determining the charge distribution in the layer. With a long relaxation time of $\tau_e = \epsilon/\sigma \approx 20$ s, the typical electric Reynold's number is also large, that is, $R_e \approx 2000$. Thus fluid convection also strongly influences the distribution of charge in the double layer. Electrification occurs when the mobile part of the double layer is entrained in the flow. This charge transport leads to charge build-up on charge-collecting insulating or isolated surfaces, eventually causing electrical discharge if leakage processes are slower than the rate of charge collection.

Streaming Electrification. The flow velocity at a stationary wall is zero. Because the Debye length λ is usually much smaller than system dimensions, such as the diameter of a pipe, the small fluid velocity within the double layer has little effect on the charge distribution, given approximately in Eq. (25). The laminar flow velocity distribution in a pipe of radius a and average velocity U is

$$v_z(r) = 2U\left[1 - \left(\frac{r}{a}\right)^2\right] \tag{27}$$

with streaming current

$$I = \int_o^a \rho(r) v_z(r) 2\pi r\, dr \tag{28}$$

Because $\lambda \ll a$, if we define $x = a - r$ as the distance from the pipe wall, the charge density is approximately that given in Eq. (25), and the velocity near the pipe wall is approximately $x\, dv_z/dr|_{r=a} = 4Ux/a$, and the streaming current is approximately

$$\begin{aligned} I &\approx \int_o^\infty \rho(x) 4Ux 2\pi\, dx \\ &= 8\pi U \rho_w \int_o^\infty x e^{-x/\lambda}\, dx \\ &= 8\pi U \rho_w \lambda^2 = -8\pi U \epsilon \zeta \end{aligned} \tag{29}$$

It is this entrained charge that can accumulate on insulating or isolated surfaces within a power transformer to cause spark discharges and occasionally lead to transformer failure.

Charge Injection Models

Schottky Emission. Schottky emission is essentially thermionic emission from a metal electrode into the conduction band of a dielectric taking into account the lowering of the work function potential barrier by the image force on the injected electron of charge $e = 1.6 \times 10^{-19}$ C. The injected current density at an absolute temperature T with an electric field E into a dielectric of permittivity ϵ is

$$\begin{aligned} J &= A_{RD} T^2 \exp\{-[\phi - (e^3 E/4\pi\epsilon)^{1/2}]/kT\}; \\ A_{RD} &= 4\pi emk^2/h^3 \sim 120\,\mathrm{A\,cm^{-2}K^{-2}} \end{aligned} \tag{30}$$

where ϕ is the work function, m is the effective electron mass, $k = 1.38 \times 10^{-23}$ J/K is Boltzmann's constant, $h = 6.6256 \times 10^{-34}$ J-s is Planck's constant and A_{RD} is the Richardson-Dushman constant of thermionic emission.

Fowler-Nordheim Field Emission. Quantum mechanical tunneling of electrons from a metal surface into a dielectric under a strong electric field results in the current density

$$J = \frac{e^3 E^2}{8\pi h\phi} \exp[-8\pi\sqrt{2m}\phi^{3/2}/3heE] \tag{31}$$

Note that in the high-field limit so that the exponential argument is much less than unity, the current density is proportional to the square of electric field E. This electric field at a metal surface is often much higher than the average electric field due to sharp surface asperities.

Avalanche Modeling

The fundamental model of electric breakdown is the avalanche model where an injected electron collides with a molecule to release an additional electron. Each of these electrons then continues with more collisions multiplying the number of electrons leading to current growth. The number of ionizing collisions per electron per unit distance is known as Townsend's first ionization coefficient α. The increase in the number density n of electrons in a distance dx is then

$$dn = n\alpha\, dx \Rightarrow n = n_0 e^{\alpha x}; \quad \alpha = e^{-v/eE\lambda}/\lambda \tag{32}$$

resulting in the number density of electrons exponentially increasing with distance, with n_o the original number of electrons at the $x = 0$ cathode. The Townsend coefficient α increases with increasing electric field E, depends strongly on the mean free path λ between collisions, and is characterized by the energy ν required to ionize gas molecules. The conduction current flow through the anode a distance d from the cathode is then

$$I(x = d) = I(x = 0) e^{\alpha d} \tag{33}$$

where $I(x = 0)$ is the cathode emission current. Such impact ionization by electrons alone is not sufficient to cause electrical breakdown.

As the fast-moving electrons enter the anode, they leave behind the relatively slower positive ions. As these positive ions drift to the cathode, they also collide with neutral molecules and liberate additional electrons with probability γ, known as Townsend's second ionization coefficient. The parameter γ also includes the effects of additional free electrons generated by photoionization processes.

The anode current then becomes

$$I(x = d) = I(x = 0) \frac{e^{\alpha d}}{1 - \gamma(e^{\alpha d} - 1)} \tag{34}$$

The current grows without bound when the denominator in Eq. (34) becomes zero so that the discharge becomes self-sustaining when

$$\gamma(e^{\alpha d} - 1) = 1 \tag{35}$$

With the mean free path λ inversely proportional to pressure, the Townsend coefficients α and γ are a function of E/p where E is the electric field and p is the gas pressure. This model is appropriate for gases, but is also used to describe electrical breakdown in liquids with formation of a gaseous bubble, per-

haps due to heating, and in solids that have voids. In a uniform electric field, the gas breakdown voltage curve vs the pressure-gap (pd) product is known as the Paschen curve, as shown in Fig. 2. For a gap of fixed spacing d, as the pressure decreases, the gas density decreases and the electron mean free path between collisions increases. Thus, each electron makes fewer collisions with gas molecules as it travels to the anode and thus avoids loss of energy due to collisions. A lower electric field can then accelerate electrons to sufficient kinetic energy for ionizing collisions. As the pressure decreases further, the breakdown voltage decreases to the Paschen minimum V_p. As the density is decreased below the Paschen minimum, there are even fewer collisions; thus self-sustaining ionization is maintained only with a corresponding increase in voltage. To the right of the Paschen minimum, there are so many collisions that much of the electron kinetic energy is dissipated hence a large voltage is necessary for ionizing collisions.

STREAMERS

Streamer Characteristics

Streamers are very fast electrical breakdown events that release large amounts of energy in a short time (18–20). Local heating due to electric field induced-charge motions can form a vapor region near the electrode. If all the electrical energy corresponding to the first current pulse in transformer oil under ac or in cyclohexane under dc is dissipated and converted to heat, the calculated gas volume compares well with observed bubble volumes. The electrical pressure is generally much higher than the local gas pressure so that continued expansion is determined by electrical forces. The process depends on the chemical composition and physical properties of the liquid, pressure and temperature, the electrode geometry, the voltage magnitude, polarity, and shape, and contaminants of air, moisture, particles, and other trace impurities. Streamers have an optical refractive index different from that of the surrounding liquid allowing visualization using shadowgraph and Schlieren photography. Their velocity depends on the liquid and voltage magnitude and polarity. The tree-like pattern of the streamer can generally be classified as slow and "bushy" for streamers emanating from the negative electrode, or fast and "filamentary" with typical diameter $\sim$10 μm for streamers emanating from the positive electrode. The addition of electron scavengers affects differently the negative and positive streamers, and their current and emitted light waveforms have similar shapes in time. Shock waves result from streamer propagation, and the streamer stops when the electric field becomes too small resulting in a string of microbubbles that dissolve in the liquid. Positive streamers are often about 10 times faster than negative streamers, although transformer oil is an exception with positive and negative streamer velocities in the same range.

As the hydrostatic pressure is increased, the electrical breakdown strength generally increases, the number and amplitude of current and light pulses are reduced, and the streamer velocity decreases. Above a threshold pressure that depends on streamer energy, the current and light pulses disappear.

At atmospheric pressure, temperature has only minor effects on streamer behavior. The number and amplitude of current and light pulses from slow streamers increase with temperature while fast filamentary streamers are unaffected by temperature. Partial discharges related to streamers seem to diminish with increasing temperature.

The quality of the electrode surface plays an important role for uniform field electrodes, but there is no significant correlation to the electrode work function for streamer initiation or breakdown voltage. Partial discharges depend greatly on properties at the metal-dielectric interface, for example, adsorbed molecules and degree of melting. The dielectric strength in liquids decreases with increasing gap spacing. For small gaps ($<$5 cm), currents for negative streamers consist of short pulses ($<$10 ns) of increasing amplitude and number during propagation. Positive streamers are generally faster than negative streamers.

In highly divergent electrode geometries under ac fields with gaps $\sim$25 mm, with a mean field $E < 40$ kV/cm, breakdown is controlled by the propagation of positive streamers whereas in moderately divergent geometries with gaps $\sim$5 mm and mean field $E < 80$ kV/cm, breakdown is controlled by negative streamers. The time to breakdown usually increases linearly with gap, while the amplitude, duration, number, and length of partial discharge streamers decrease with increasing gap.

Investigation of a number of silicone fluids of identical chemical nature but with viscosity varying from 10 to 10,000 cSt, found no significant change of streamer velocity or shape (20). Similar results including no significant change in the time to breakdown have been found for polydimethylsiloxanes also varying by a factor of 1000 in viscosity. These results indicate that viscosity has little effect on the breakdown process.

Most streamers appear to be the same whatever the liquid. There is virtually no dependence on the thermal properties of specific heat and heat of vaporization, physical properties of surface tension, compressibility, viscosity, or vapor pressure, electrical properties of charge mobilities and lifetimes, or optical properties.

Prebreakdown Cavity Expansion

Optical studies show that the prebreakdown process begins with the formation of a rapidly expanding vapor cavity adjacent to an electrode. A current pulse provides the energy that is converted into heat that evaporates the liquid dielectric. Expansion of the cavity due to electric field forces is limited by liquid inertia and viscosity. Simplified analysis assumes that the cavity region is a highly conductive ionized plasma that puts the cavity surface at the same potential V as the contacting electrode (21,22).

A simple electrohydrodynamic model equates the kinetic energy of the spherically expanding cavity to the work done by the electric field. For fluid of mass density ρ_d, permittivity ϵ, cavity radius $R(t)$, and wall velocity $U = dR/dt$, the kinetic energy is

$$KE = 2\pi\rho_d U^2 R^3 = 2\pi\rho_d R^3 \left(\frac{dR}{dt}\right)^2 \tag{36}$$

For a spherical conductor of radius R, a distance a above a ground plane the surface electric field can be approximated

as

$$E(R) = \frac{V}{R(a/R)^{1/4}} \tag{37}$$

so that the electric pressure is

$$P_e(R) \approx \frac{1}{2}\epsilon E^2(R) \approx \frac{1}{2}\frac{\epsilon V^2}{a^{1/2}R^{3/2}} \tag{38}$$

The electric work done in expanding the cavity from radius 0 to radius R is then

$$W_e = \int_0^R P_e(r)4\pi r^2\,dr = \frac{4\pi}{2}\frac{\epsilon V^2}{a^{1/2}}\int_0^R r^{1/2}\,dr = \frac{4}{3}\frac{\pi\epsilon V^2}{a^{1/2}}R^{3/2} \tag{39}$$

Equating this work to the kinetic energy yields

$$R(t) = \left[\frac{49\epsilon V^2}{24\rho_d a^{1/2}}\right]^{2/7} t^{4/7} \tag{40}$$

Comparison of this predicted radial expansion to measurements in such fluids as hexane and silicone fluids provides reasonably good agreement.

In the high-viscosity limit the kinetic energy can be neglected and the electrical work is converted to viscous power dissipation given by

$$P_v = 32\pi\eta R U^2/3 = 32\pi\eta R\left(\frac{dR}{dt}\right)^2 \Big/ 3 \tag{41}$$

The electric power is given by

$$P_{\text{elec}} = \frac{dW_e}{dt} = \frac{2\pi\epsilon V^2}{a^{1/2}}R^{1/2}\frac{dR}{dt} \tag{42}$$

Equating the electrical power and viscous dissipated power yields

$$R(t) = \left[\frac{q\epsilon V^2}{32\eta a^{1/2}}\right]^{2/3} t^{2/3} \tag{43}$$

Representative cavity growth and resulting surface instabilities are shown in the Schlieren pictures of Fig. 6 using an image converter camera. Negative and positive point electrodes are 3 mm above a ground plane with toluene as the dielectric liquid. The negative streamer shows significant surface instability.

Electrohydrodynamic Instability of the Cavity

As the cavity expands, surface instabilities lead to interfacial fingers that either grow into streamers or bush-like growths. There are two limiting cases of interest defined by an inertial time constant $\tau_i = \rho_d/k^2\eta$ and an electroviscous time constant $\tau_v = 2\eta/\epsilon E^2$, where $k = 2\pi/\lambda$ is the wavenumber of an assumed sinusoidal interfacial displacement $\xi(x,t)$ with wavelength λ of the form

$$\xi(x,t) = \text{Re}[\hat{\xi}e^{st-jkx}] \tag{44}$$

Here, $\hat{\xi}$ is the complex amplitude of the interfacial displacement, s is the growth rate with the system being unstable if the real part of s is positive, and x is the coordinate along the interface.

At the start of the process, the system is limited by fluid inertia and the growth rate of the instability is

$$s_i = k[\epsilon E^2/2\rho_d]^{1/2} \tag{45}$$

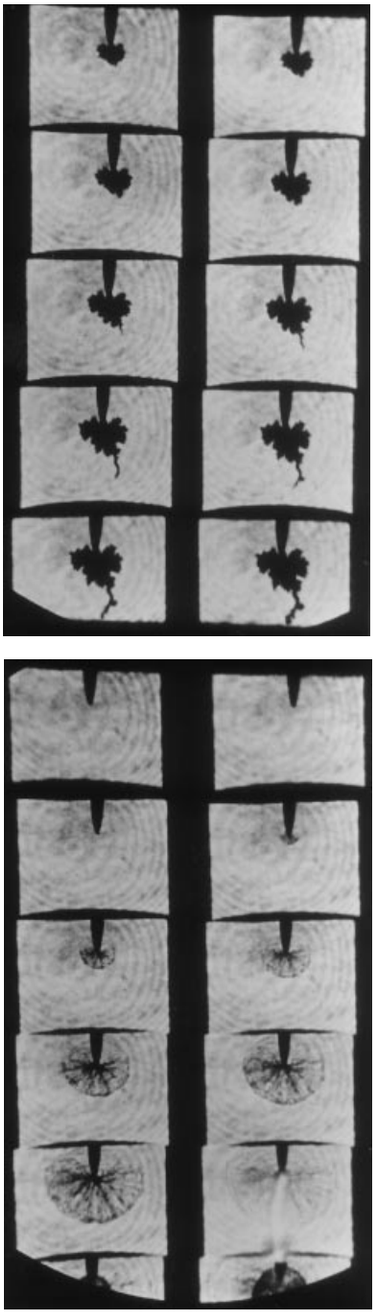

(a)

(b)

Figure 6. Schlieren image converter photographs of prebreakdown cavity growth and instability in toluene for (a) a negative needle at 25 kV pulse and (b) a positive needle at 35 kV pulse. The voltage pulse has duration of about 10 μs and the needle is 3 mm above a ground plane. The images for each sequence start at the upper left, and alternate left to right downward with 200 ns between frames. Photographs supplied by Dr. E. F. Kelley of the U.S. National Institute of Standards and Technology.

As the interface deforms to shorter wavelength disturbances, the viscous losses increase, thus driving the system into the viscous limited regime with growth rate

$$s_v = \epsilon E^2/4\eta \tag{46}$$

The transition between inertial and viscous regimes approximately occurs when $\tau_v = \tau_i$, which occurs at critical wavenumber

$$k_c = [\epsilon E^2 \rho_d/2\eta^2]^{1/2} \tag{47}$$

At this wavenumber, the critical inertial growth rate is

$$s_c = \epsilon E^2/2\eta \tag{48}$$

This simple and approximate combination of hydrodynamic and electrostatic concepts agreed reasonably well with observations of the growth rate and surface deformation periodicity $\lambda_c = 2\pi/k_c$ of the initial development of streamers.

Hydrodynamic Shock Wave Propagation After Electrical Breakdown. Once electrical breakdown initiates from the tree-like cavity, there is a radial expansion of both an acoustic shock wave and of the conductive breakdown channel as shown in Figs. 7 and 8. The acoustic shock wave expands at a constant velocity while the expanding radius of the breakdown channel is proportional to the fourth root of energy and the square root of time. These dependencies are predicted by modeling the breakdown channel as an expanding adabatic ideal gas with an instantaneous input of energy per unit length $\mathscr{E}$ (23). The thermodynamic Rankine–Hugoniot boundary conditions in the strong shock limit are used to relate discontinuities in velocity, pressure, and mass density across the cylindrical shock front using the same analysis as that employed to describe exploding wires and lightning in air. When the expansion velocity of the gas column decreases below the acoustic wave velocity, an acoustic wave propagates ahead of the electrohydrodynamic shock.

Under typical experimental conditions, powers on the order of 2 MW are dissipated within a 1 mm diameter plasma column of 5 mm length in about 500 ns. Graphitic structures have been identified by transmission microscopy of residues removed from the liquids after several breakdowns that imply spark temperatures in excess of 1400°C. Such high temperatures cause vaporization of the liquid dielectric.

The analysis solves the conservation of mass, momentum, and energy equations for an inviscid and compressible adiabatic ideal gas for one-dimensional cylindrical radial expansion. It is found that the radial position and velocity of the shock front are

$$\begin{aligned} R &= \alpha\sqrt{t} \\ U &= \frac{dR}{dt} = \frac{\alpha}{2\sqrt{t}}; \quad \alpha = [2\mathscr{E}/(\pi\rho_d T(\gamma))]^{1/2} \end{aligned} \tag{49}$$

where $\mathscr{E}$ is the total instantaneous energy per unit length input to the streamer at $t = 0$ and $T(\gamma)$ is an energy integral of the expansion work due to pressure and the kinetic energy, where $\gamma = c_p/c_v$ is the ratio of specific heats in the streamer. Particular values of $T(\gamma)$ are

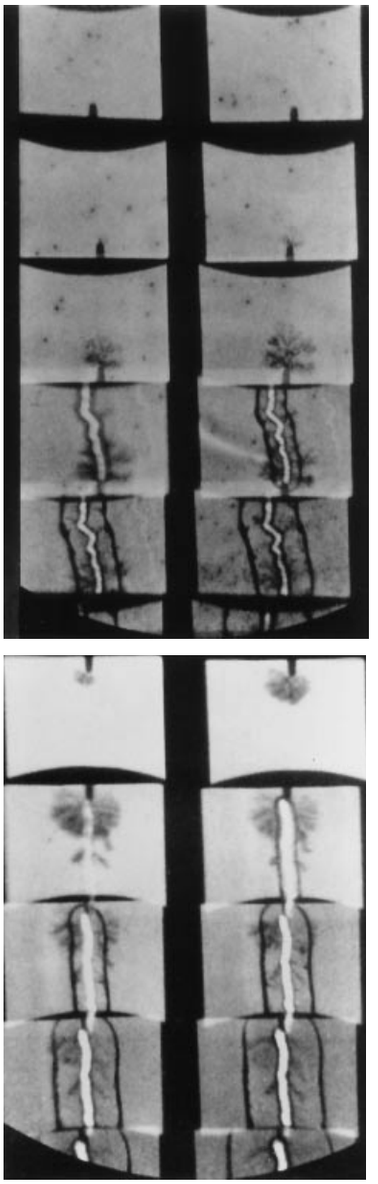

(a)

(b)

Figure 7. Image converter camera Schlieren measurements showing representative cavity, surface instability, streamer formation, streamer radial expansion and hydrodynamic acoustic shock wave for (a) a negative needle with a 135 kV pulse of 2 μs duration and (b) a positive needle for a 141 kV 2 μs pulse. The time between frames is 210 ns and the electrode gap is 3 mm. The negative streamer in (a) takes 840 μs to cross the gap while the positive streamer in (b) takes only 520 ns to cross the gap. Photographs supplied by Dr. E. F. Kelley of the U.S. National Institute of Standards and Technology.

$$\begin{aligned} T(1.66) &\approx 0.36 \text{ (monatomic gas)} \\ T(1.4) &\approx 0.63 \text{ (air)} \\ T(1.08) &\approx 3.2 \text{ (}n\text{-hexane vapor)} \end{aligned} \tag{50}$$

Electrical breakdown measurements made in transformer oil using needle-sphere electrodes with a 1.6 mm gap and needle stressed by +19.8 kV peak potential are plotted in Fig. 9 from optical Schlieren measurements of the expanding streamer and acoustic wave like that in Fig. 8. The first frame in Fig.

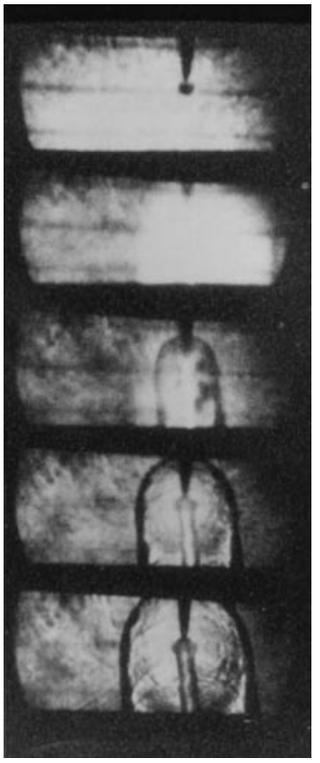

Figure 8. Five image converter camera frames taken at 1 μs intervals showing the electrical breakdown events in transformer oil using needle-sphere electrode geometry with 1.6 mm gap. The needle is at a positive 19.8 kV voltage.

8 shows a branching tree structure emanating from the needle. The second frame shows the light spark discharge. In the third through fifth frames, the acoustic wavefront and central spark are expanding radially.

The results of many measurements are shown in Fig. 9(a). The open circles show that the acoustic wave expands at a constant radial velocity of $\approx 1.5 \times 10^5$ cm/s, which is in good agreement with the speed of sound in transformer oil of $\sim 1.4 \times 10^5$ cm/s at standard temperature and pressure. The solid circles on a ten-to-one decreased radial scale are in good agreement with Eq. (49) shown as a dashed line. Figure 9(b) shows that the parameter α is proportional to the square root of voltage, as confirmed by measurements in *n*-hexane, isooctane, cyclohexane and toluene (24). The best fit to the data in Fig. 9 is $\alpha = 0.17$ m/$\sqrt{\text{s}}$ corresponding to an energy per unit length of $\mathscr{E} = \pi\rho_d T(\gamma)\alpha^4/2 = 3.8$ J/m taking $\rho_d \approx 900$ kg/m^3 and $T(\gamma) \approx 3.2$. The total spark energy over the 1.6 mm electrode gap is ≈ 6 mJ.

Spectral Characteristics

In addition to shadowgraph and Schlieren photographic techniques used to observe and measure propagation velocities of prebreakdown bubble streamer events, photomultiplier methods record integrated light while spectral analysis and chromatographic analysis correlate electrical excitation, streamer development, and generated gases.

Spectroscopic studies of emitted light during the prebreakdown phase of hydrocarbon liquids under lightning impulse voltages extend from the UV to visible range (25). In *n*-hexane, the light revealed atomic and molecular hydrogen and carbon C_2 and C_3 molecules, together with small amounts of electrode metal. The formation of these species was attributed to an electron avalanche mechanism similar to gas discharges.

Other work used a blend of mono- and dibenzyl toluene (M/DBT) and phenyl xylylethane (PXE) that was initially degassed and then saturated with nitrogen, which was then subjected to tens of thousands of rectangular voltages in a point-plane geometry to generate streamers. The liquid samples were then analyzed by gas chromatography to identify the nature and proportion of the gases generated by streamers. Measured gases included H_2, CH_4, C_2H_4, C_2H_6, and C_2H_4, and were higher in volume for positive streamers than for negative streamers (26).

Effects of Additives

Small concentrations of polyaromatic compounds greatly reduce the dielectric strength of a napthenic oil, either due to an increase in streamer velocity or to a decrease in the initiation voltage (27). The addition of a nonionic electronic scavenger such as SF_6 or ethyl chloride to a napthenic oil or 2,2,4-trimethylpentane makes the negative streamers more filamentary and up to five times faster. Negative streamer velocities in cyclohexane increase by a factor of 10 with 0.04 mol/L of CCl_4 (28,29). There are no detectable effects on positive streamers. Negative streamers, which are usually "bushy," become more filamentary and closely resemble positive streamers with the addition of electron scavengers that speed up negative streamers. The addition of a nonionic low ionization potential compound such as *N*,*N*′-dimethylaniline (DMA) has no effect on negative streamer velocity but does increase positive streamer velocity up to three times in a napthenic oil and in 2,2,4-trimethylpentane. The addition of low ionization potential tetramethylparadiphenylamine (TMPD) or DMA to cyclohexane does not change the streamer shape but does increase the velocity by a factor less than two. Positive streamers increase their velocity by three and become more filamentary. Ionic additives such as picrate of triisomylammonium (TIAP) and Aerosol OT [sodium di(2-ethylhexyl)sulfosuccinate(13)] typically increase the velocity of positive and negative streamers up to a factor of 10. Additives also change the shape and amplitude of currents for slow negative streamers.

Measurements

In a typical experimental system, a pulsed high voltage is applied to a needle electrode above a ground plane. An image converter camera with picture repetition rate of $\sim 2 \times 10^7$ Hz and frame exposure time of 10 or 100 ns permits optical recording of the streamer propagation by shadowgraph or Schlieren photography. A point-to-point electrode geometry permits simultaneous observation of positive and negative streamers.

Positive Point Electrode. In the vicinity of the positive point electrode, electrons in the fluid are attracted to the anode locally heating the liquid to cause a low-density region that causes branches in the positive streamer. Inside this low-density region, fluid molecules are further ionized to generate more free electrons attracted to the anode. The remaining

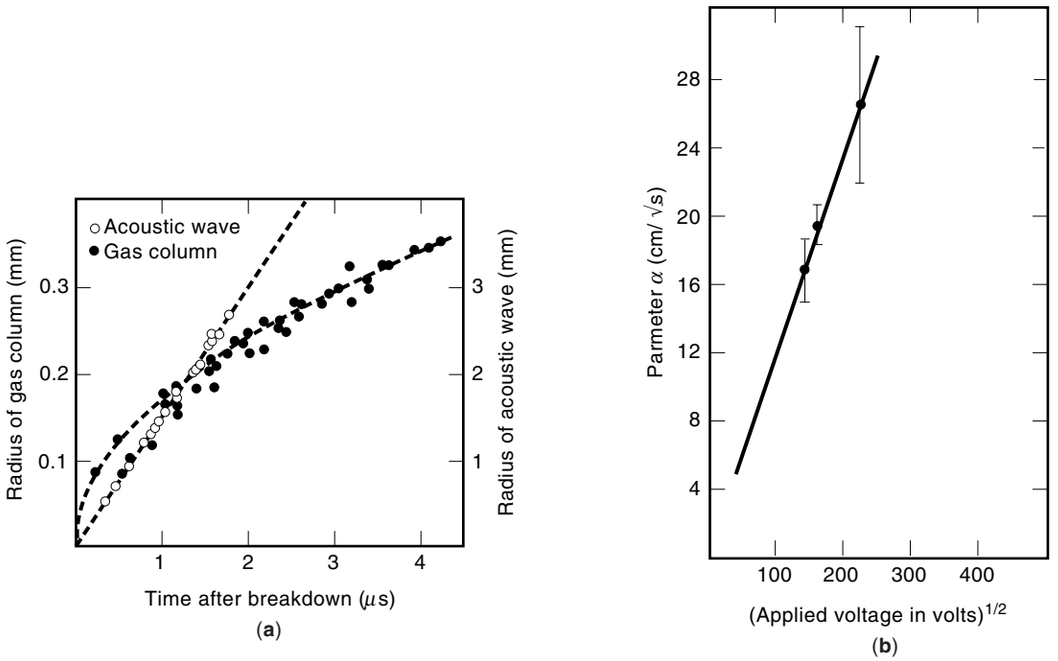

Figure 9. (a) The measured radii of the acoustic and gaseous shock waves versus time for experiments in transformer oil with the needle electrode at +19.8 kV relative to the sphere electrode with 3 mm gap. Note that the radial scale for the acoustic wave and for the gaseous shock wave differ by a factor of ten. The curved dashed line is the function $R = \alpha\sqrt{t}$ for $\alpha = 0.17$ m/$\sqrt{\text{s}}$. The straight dashed line indicates an acoustic wave velocity of 1.5×10^5 cm/s; (b) The parameter α is seen to vary as $\sqrt{V}$, for needle voltages of +20 kV, +24 kV, and −49 kV.

positive ions build up a space-charge field that decreases the electric field near the needle, in effect acting to make the effective needle tip larger. The initiation field strength for positive streamers in transformer oil is about $E_+ \sim 2 \times 10^8$ V/m. The average streamer velocity is $\sim 1 - 3$ km/s. As the positive streamer approaches the cathode, the electric field ahead of the streamer is increased due to the positive space charge in the streamer. This leads to very fast events that bridge the remaining gap and initiate electrical breakdown.

At higher field levels of order $1.2 - 1.6 \times 10^9$ V/m, secondary streamers can emanate from primary streamers and propagate with velocities of order $11 - 32$ km/s, giving a reduced time to breakdown. The streamer branch diameters are $\sim 80 - 90$ μm. Highly overstressing the gap further causes a short primary streamer, an earlier secondary streamer inception, and an ultrahigh-speed tertiary streamer that is often self-luminous. The time to breakdown for an 11 mm point-plane gap in transformer oil is ~275 ns.

Negative Point Electrode. Electrons are injected into the liquid from a high-field stressed point electrode, again causing local heating to a low-density region. The negative streamer typically requires an initiation field $E_- > 2.5 \times 10^8$ V/m. The streamer can travel as fast as 100 km/s. The primary negative streamer has only one or two main branches at low fields, growing towards the anode like a leafless tree at a velocity up to ~1 km/s with branch diameters $\sim 30 - 70$ μm. At higher fields, the streamer appears as a compact bushy structure with many branches propagating with velocities about $1 - 3.5$ km/s. At very high fields the primary streamer is very filamentary, traveling more than 80 km/s.

RF Voltage Tests. Because at high frequencies one half-cycle is too short to allow streamers to bridge the gap, positive and negative streamers are formed alternately each half-cycle with point-plane electrodes. On the positive needle half-cycle, a positive primary streamer initiates when the streamer inception voltage is exceeded. When the voltage falls below the extinction voltage, the streamer stops with a decay in brightness. As soon as the voltage crosses zero and reaches initiation voltage, a negative streamer forms at the needle tip.

Long Gaps. To keep breakdown voltages at moderate levels, gaps are generally small, of millimeter order. Such short path lengths with typical streamer velocities of order 1 km/s result in propagation times of microsecond order. Longer paths with up to 1 m gap typically have lower average breakdown field strengths, allow greater time and spatial resolution of streamer processes, and have streamer properties relatively independent of electrode geometry. Recently reported results have used impulse voltages with gaps up to 35 cm and ac voltages with gaps up to 80 cm (30,31). Positive streamers have been of most interest because they most often lead to breakdown. Negative streamers are less branched and travel about 10 times faster than positive streamers (32). Typical electrode geometries include point- or rod-to-plane gaps as well as sphere-plane gaps. The main difference of prebreakdown phenomena in large gaps over small gaps is the apparent stepped character of the propagation observed in streak recordings (33). The recordings show bright light flashes, presumably due to fast gas discharges, that periodically reilluminate the discharge channel at each step (34). For long impulse voltages, the average propagation speed of ~2

km/s is the same for long and short gaps. Below the breakdown voltage, streamer stopping lengths increase linearly with inception voltages. There seems to be a critical distance beyond which streamers never stop, presumably due to the increased electric field at the streamer tip as it approaches the plane electrode that counteracts the voltage drop along the streamer channel.

Electrical Current and Light Emission

Transient current pulses are generally accompanied by light emission pulses. The current signal is often measured using a storage oscilloscope of the voltage across a noninductive resistor in series with the test cell and the light is detected by a photomultiplier tube or other optical detector. The important quantity is the magnitude of the charge corresponding to the time-integration of each pulse of current as it gives information on the nature of the discharge, on the propagation mode, and on the physicochemical mechanisms.

In a point-plane electrode geometry the current of a slow bush-like streamer consists of irregularly spaced bursts, the amplitude of which generally increases with the time of streamer propagation. The emitted light has a similar shape in time to the current. The number and amplitude of both streamer current and emitted light pulses increase as the voltage is increased.

The light emitted by a fast filamentary streamer consists of a unique pulse, while the current has a dc level on which are superimposed other pulses. The amplitude of the current and light pulses increase with the streamer propagation velocity. The currents of fast streamers are always higher than those of slow ones, independent of polarity and liquids. For long gaps (5 to 100 cm) and for both polarities, the current consists of irregularly spaced current pulses. The current and emitted light waveforms of both negative and positive streamers under ac voltages are similar to those observed under impulse and step voltages.

SPACE-CHARGE EFFECTS

Space-Charge Distortion of the Electric Field

Many analytical models assume that the electric field is spatially uniform. This motivates many tests to use parallel plane electrodes, but the uniform field assumption is only true in the central region between electrodes in the absence of net volume charge.

To help understand space-charge effects, often due to charge injection from electrodes, consider the simplest case of planar electrodes with an x directed electric field E that is distorted by net charge density $\rho(x)$ dependent only on the x coordinate. In such a one-dimensional electrode geometry, Gauss's law of Eq. (2) requires that the slope of the electric field distribution be proportional to the local charge density:

$$\nabla \cdot \mathbf{E} = \frac{\rho}{\epsilon} \rightarrow \frac{\partial E}{\partial x} = \frac{\rho}{\epsilon} \tag{51}$$

For the case of no volume charge shown in Fig. 10(a), the electric field is uniform given by $E_o = V/d$ for a voltage V across a gap d. The electric field drops at a charge-injecting electrode, but its average value E_o remains constant at V/d. Charge injection thus causes the electric field to increase above the average value at the noncharge-injecting electrode. In Fig. 10(b), unipolar injection has the electric field maximum at the noncharge-injecting electrode, thus possibly leading to electrical breakdown at lower voltages. For bipolar homocharge injection in Fig. 10(c), positive charge is injected at the anode and negative charge is injected at the cathode; thus the electric field is lowered at both electrodes and is largest in the central region. As electrical breakdown often initiates at the electrode-dielectric interface, this case can allow higher voltage operation without breakdown, being up to ~40% higher in highly purified water (15). If the voltage suddenly reverses, the electrical field must also instantaneously reverse, but the charge distribution cannot immediately change because it takes some time for the volume charge to migrate. Thus, for early times with voltage reversal, positive charge is near the cathode and negative charge is near the anode, enhancing the fields near the electrodes as shown in Fig. 10(d). Such a bipolar heterocharge configuration leads to breakdown at lower voltages as has been found in HVDC polyethylene cables when the voltage is instantaneously reversed to reverse the direction of power flow. A similar configuration to Fig. 10(d) also occurs in ionized dielectric liquids where free ions are attracted to their image charges on the electrodes.

Drift-Dominated Unipolar Conduction

Governing Equations of Mobile Charge. Because ohmic conduction involves the presence of equal amounts of positive and negative charge, there can be a net current flow with zero volume charge. However, a volume charge distribution within a dielectric can arise from spatially varying conductivity, irradiation, charge injection from high field-stressed electrodes, dielectric ionization, or by contact charging of impurities.

To model net charge transport, a drift-dominated unipolar mobility model is used where the velocity $d\mathbf{r}/dt$ of a positive charge carrier is proportional to the local electric field through the mobility μ, $d\mathbf{r}/dt = \mu\mathbf{E}$, and in turn the electric field is related to the charge density through Gauss' law of Eqs. (2) and (51) (35).

Consider a one-dimensional model in a medium of thickness d and permittivity ϵ with x directed electric field E. Without loss of generality we assume that positive mobile charge with density ρ has a mobility μ. The current density constitutive law is then

$$\mathbf{J} = \rho\frac{d\mathbf{r}}{dt} = \rho\mu\mathbf{E} \tag{52}$$

Substituting Eq. (52) into Eq. (3) and integrating with respect to x together with one-dimensional forms of Eqs. (1) and (2) yield the governing equations

$$\epsilon\frac{\partial E}{\partial t} + \rho\mu E = J(t) \tag{53}$$

$$\frac{\partial E}{\partial x} = \frac{\rho}{\epsilon} \tag{54}$$

$$v = \int_0^d E\,dx \tag{55}$$

where $J(t)$ is the terminal current per unit electrode area and v is the voltage difference across the electrodes at $x = 0$ and

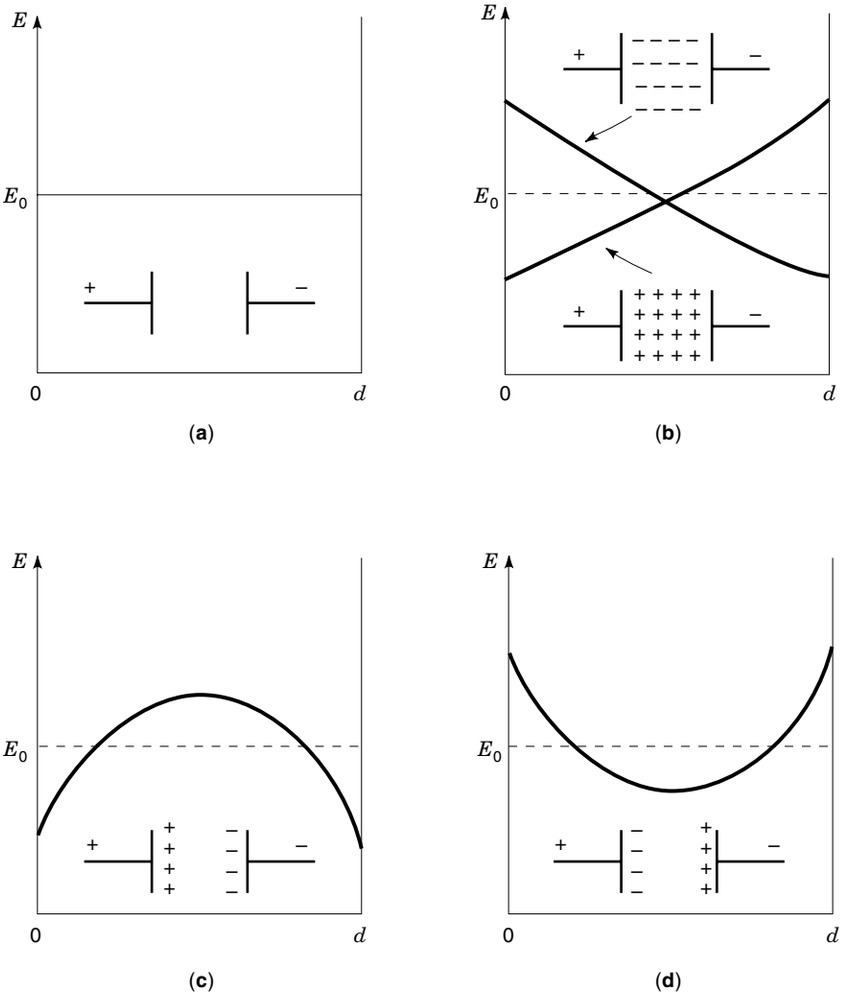

Figure 10. Space-charge distortion of the electric-field distribution between parallel-plate electrodes with spacing d at voltage v so that the average electric field is $E_0 = v/d$. (a) No space charge so that the electric field is uniform at E_0; (b) unipolar positive or negative charge injection so that the electric field is reduced at the charge-inducing electrode and enhanced at the noncharge-injecting electrode; (c) bipolar homocharge injection so that the electric field is reduced at both electrodes and enhanced in the central region; (d) bipolar heterocharge distribution where electric field is enhanced at both electrodes and depressed in the central region.

$x = d$. Differentiating Eq. (53) with respect to x and using Eq. (54) gives an equation for the charge density

$$\frac{\partial \rho}{\partial t} + \frac{\rho^2 \mu}{\epsilon} + \mu E \frac{\partial \rho}{\partial x} = 0 \tag{56}$$

Using Eq. (54) in Eq. (53), integrating between the electrodes, and then using Eq. (55) yields the terminal voltage–current relationship

$$\frac{dv}{dt} + \frac{\mu}{2}[E^2(x = d) - E^2(x = 0)] = \frac{J(t)d}{\epsilon} \tag{57}$$

The first term is proportional to the familiar capacitive displacement current while the second term is due to migrating charge.

Equations (53) and (56) are a pair of quasi-linear hyperbolic partial differential equations that can be converted to a set of ordinary differential equations by jumping into the frame of reference of the migrating charge moving at the charge velocity

$$\frac{dx}{dt} = \mu E \tag{58}$$

In this moving frame of reference, the total time derivatives of electric field and charge density are

$$\frac{dE}{dt} = \frac{\partial E}{\partial t} + \frac{dx}{dt}\frac{\partial E}{\partial x} = \frac{J(t)}{\epsilon} \tag{59}$$

$$\frac{d\rho}{dt} = \frac{\partial \rho}{\partial t} + \frac{dx}{dt}\frac{\partial \rho}{\partial x} = -\frac{\rho^2 \mu}{\epsilon} \tag{60}$$

The solution to Eq. (60) is

$$\rho(t) = \frac{\rho_0(t = t_0)}{[1 + \rho_0(t = t_0)\mu(t - t_0)/\epsilon]} \quad \text{on} \quad \frac{dx}{dt} = \mu E \tag{61}$$

where $\rho_0(t = t_0)$ is the initial charge density on a trajectory that starts at time $t = t_0$. Physically, this solution of decreasing charge density with time is due to the self-field Coulombic repulsion of charge so that any initial packet of charge expands with time. Even though the total charge within a packet is constant, the density decreases because the volume of charge is increasing. Note that if the initial charge density $\rho_0(t = t_0)$ is zero, the charge density remains zero along the charge trajectory.

If the terminal current density $J(t)$ is known, the electric field along a charge trajectory is obtained by direct time inte-

gration of Eq. (59) and the position of the charge is found by time integration of the electric field using Eq. (58). Often the terminal voltage is constrained so that the terminal current must be found using Eq. (57). Because the electric field at both electrodes is generally not yet known, usually a numerical method is needed to self-consistently solve for all variables.

Dc Steady-State Distributions. The dc steady-state distributions for electric field and charge density are found by setting the time derivatives in Eqs. (53) and (56) to zero

$$E_{ss} = \left[\frac{2Jx}{\epsilon\mu} + E_0^2\right]^{1/2} \tag{62}$$

$$\rho_{ss} = \frac{J}{\mu E_{ss}} = \frac{\epsilon dE_{ss}}{dx} = \frac{J}{\mu}\left[\frac{2Jx}{\epsilon\mu} + E_0^2\right]^{-1/2} \tag{63}$$

where J is the dc steady-state current density and E_0 is the emitter electric field at $x = 0$, which must be specified as a charge-injection boundary condition, such as from Eqs. (30) or (31).

The current/voltage relation is found from Eq. (57) by integrating Eq. (62) between electrodes stressed by dc voltage V

$$V = \int_0^d E_{ss}\,dx = \frac{\epsilon\mu}{3J}\left\{\left[\frac{2Jd}{\epsilon\mu} + E_0^2\right]^{3/2} - E_0^3\right\} \tag{64}$$

Simplifying Eq. (64) gives

$$\frac{16Jd^3}{\epsilon\mu V^2} = 9 - 12\left(\frac{E_0 d}{V}\right)^2 + \left\{\left[9 - 12\left(\frac{E_0 d}{V}\right)^2\right]^2 + 192\left(\frac{E_0 d}{V}\right)^3\left[1 - \frac{E_0 d}{V}\right]\right\}^{1/2} \tag{65}$$

For positive charge injection the emitter electric field E_0 must obey the inequality $0 \le E_0 \le V/d$. For negative E_0 there is no charge injection as the electric field would push the positive charge back into the electrode. For $E_0 > V/d$, the spatial derivative of E_{ss} could not be positive as required by Gauss' law of Eq. (54) for positive charge injection and simultaneously satisfy Eq. (55) of having an average field strength between electrodes of V/d. The positive space-charge distribution distorts the electric field so that the maximum electric field strength occurs at the negative electrode at $x = d$. This field enhancement is important in electric breakdown studies as breakdown initiates where the electric field is largest.

The largest electric field at the noncharge emitting electrode at $x = d$ is $E(x = d) = 1.5\ V/d$ which occurs for space-charge limited conditions when $E_0 = 0$ and $\rho_{ss}(x = 0) = \infty$, so that $Jd^3/\epsilon\mu V^2 = 9/8$. As $E_0 d/V$ approaches unity, the electric field distribution approaches a uniform field as the injected charge density and current density become small.

We expect that the injected charge density at $x = 0$, $\rho_{ss}(x = 0) = \rho_0$ would increase as the electric field E_0 at the charge-injecting electrode increases. The simplest relationship that approximates Eq. (31) in the high-field limit when the exponential is approximately unity is

$$\rho_0 = AE_o;\ A \approx \frac{e^3}{8\pi h\phi\mu} \tag{66}$$

where A is an injection constant. The steady-state current density which is independent of x can be particularly evaluated at $x = 0$ as

$$J = \rho\mu E = \rho_0\mu E_o = \mu A E_o^2 \tag{67}$$

Using Eq. (67) in Eq. (64) lets us solve for E_0 as

$$\frac{E_o d}{V} = \frac{3Ad/\epsilon}{(2Ad/\epsilon + 1)^{3/2} - 1} \tag{68}$$

Drift-Dominated Conduction in Pulse Power Technology. Highly purified water and water/ethylene glycol mixtures have been studied for use as the dielectric in pulse-forming transmission lines as shown in Fig. 4 because the high relative dielectric constant $\epsilon_r \approx 40 - 88$ and high resistivity $18 - 8500$ MΩ-cm, allow short and efficient low-impedance transmission lines, especially at ~ -35°C with a mixture of 60% glycol/40% water.

In testing such pulse-forming lines it was found that at high electric stress, the open-circuit voltage across immersed parallel plate electrodes decayed more quickly as the initial voltage increased and that the decay rate depended on electrode spacing and was not exponential as shown in Fig. 11(a) and (b) for two different initial voltages (15,16,35). This disagrees with the simple ohmic model of a lossy homogeneous capacitor where the open- circuit decay is exponential with decay rate $\tau = RC = \epsilon/\sigma$ independent of capacitor geometry and voltage as given by Eq. (5).

To explain the nonlinear behavior we use the unipolar ion conduction law of Eq. (52) where in a qualitative sense, the quantity $\rho\mu$ is an effective conductivity that varies with time and position. In addition to the dielectric relaxation time, there is a time of flight time constant $t_d = d^2/(\mu V)$ for injected charge to reach the opposite electrode, which depends on electrode spacing and voltage.

To emphasize space-charge effects we assume that the ohmic conductivity is zero and take the capacitor to be initially uncharged in the dielectric volume but with an initial applied voltage v at $t = 0$ and then open circuited thereafter. We find the injection electric field at $x = 0$, $E_0(t)$, using Eq. (53) with $J(t) = 0$ and the linear charge injection law of Eq. (66)

$$\frac{dE_0}{dt} + \frac{A\mu}{\epsilon}E_0^2 = 0 \Rightarrow E_0(t) = \frac{v/d}{1 + A\mu v t/\epsilon d} \tag{69}$$

where the initial condition is $E_0(t = 0) = v/d$.

For those trajectories of injected charge that start at $x = 0$ at time $t = t_0$, Eq. (59) with $J(t) = 0$ shows that the electric field along the trajectory remains constant at the $x = 0$ emitter electric field, $E(t) = E_0(t = t_0)$. Then the trajectory is given from Eq. (58) as

$$\frac{dx}{dt} = \mu E_0(t = t_0) \Rightarrow x(t) = \mu E_0(t = t_0)(t - t_0) = \frac{(\mu v/d)(t - t_0)}{[1 + A\mu v t_0/\epsilon d]} \tag{70}$$

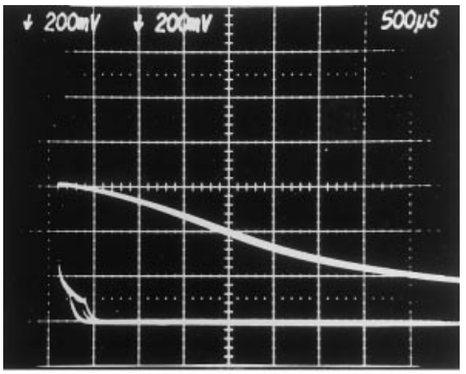

(a)

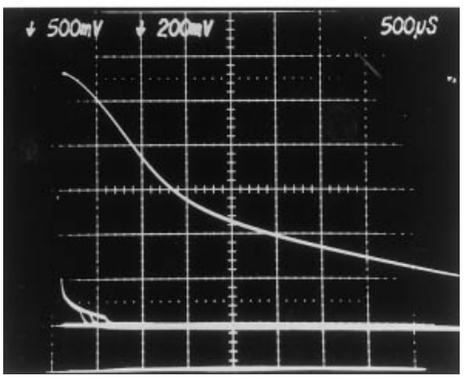

(b)

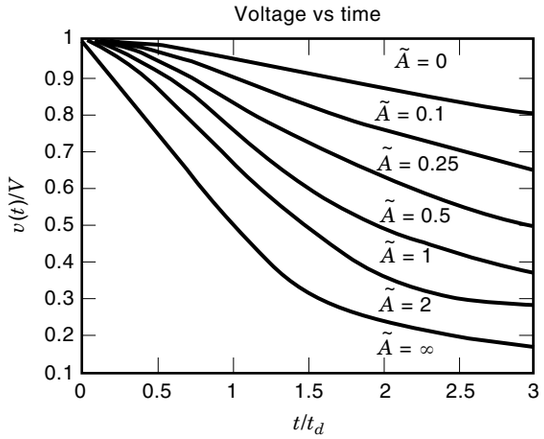

(c)

Figure 11. Measured open-circuit voltage decay vs time for an 80% ethylene glycol/20% water mixture at −10°C with a dielectric relaxation time ~24 ms for parallel-plate stainless-steel electrodes with 5.1 mm gap with initial voltages of (a) 55 kV and (b) 90 kV. Note the change in sign of the curvature of both traces at early time and that by $t \approx 4.5$ ms, both voltages are about the same despite the large difference in initial voltage. (c) Theoretical curves of Eq. (75) using a drift-dominated unipolar conduction model for various values of positive charge injection parameter $\tilde{A} = Ad/\epsilon$ showing nonexponential open-circuit voltage decay.

In particular, the trajectory that starts at $t_0 = 0$ defines the migrating charge front that reaches $x = d$ at time t_d

$$x_d(t) = \frac{\mu v t}{d}; t_d = \frac{d^2}{\mu v} \tag{71}$$

Solving Eq. (70) for t_0 gives

$$t_0 = \frac{\mu v t/d - x}{(\mu v/d)(1 + Ax/\epsilon)} \tag{72}$$

so that the electric field and charge density at time t and position x are

$$E(x,t) = \begin{cases} \dfrac{v(1+Ax/\epsilon)}{d(1+Adt/\epsilon t_d)}, & 0 \le x \le x_d(t) \\ v/d, & x_d(t) < x < d \end{cases} \tag{73}$$

$$\rho(x,t) = \epsilon \frac{\partial E}{\partial x} = \begin{cases} \dfrac{Av/d}{1+Adt/\epsilon t_d}, & 0 < x < x_d(t) \\ 0, & x_d(t) < x < d \end{cases} \tag{74}$$

The terminal voltage is then computed as

$$v(t) = \int_0^d E dx = \int_0^{x_d(t)} E dx + \int_{x_d(t)}^d E dx = \begin{cases} v\left[1 - \dfrac{Adt^2}{2\epsilon t_d^2(1+Adt/\epsilon t_d)}\right], & 0 \le t \le t_d \\ \dfrac{v(1+Ad/2\epsilon)}{1+Adt/\epsilon t_d}, & t \ge t_d \end{cases} \tag{75}$$

Figure 11(c) shows the nonexponential decay of Eq. (75) for various values of charge-injection constant A, which has similar shape to the measurements shown in Fig. 11(a) and (b).

Electrohydrodynamic Mobility. The Coulombic force on net space charge in the fluid gives rise to turbulent fluid motions causing convection currents in addition to conduction currents. The viscous diffusion time $\tau_v = \rho_d d^2/\eta$ determines whether fluid inertia with mass density ρ_d or fluid viscosity η dominates fluid motions over a characteristic length d. Water, with a room-temperature fluid density of $\rho_d \cong 10^3$ kg/m^3 and viscosity of $\eta \cong 10^{-3}$ N·s/m^2, has $\tau_v \cong 100$ s over a characteristic length of $d = 1$ cm. Since this viscous diffusion time is very large compared to the dielectric relaxation time $\tau_e = \epsilon/\sigma \cong 600$ μs (at T = 0°C) and representative charge migration times $\tau_{\text{mig}} \cong d/\mu E \cong 4$ ms (for hydronium ion at 10°C with $\mu = 2.9 \times 10^{-7}$ m^2/V·s) based on a field of 100 kV/cm, fluid motions are essentially limited by their own inertia.

The ion mobility may also be enhanced by electrohydrodynamic motions (36). If the change in kinetic fluid energy equals the electrostatic field energy

$$\frac{1}{2}\rho_d v^2 = \frac{1}{2}\epsilon E^2 \tag{76}$$

the electrohydrodynamic mobility is

$$\mu_{EHD} = \frac{v}{E} = \sqrt{\epsilon/\rho_d} \tag{77}$$

For water [$\epsilon = 80\epsilon_0$, $\rho_d = 1000$ kg/m^3], $\mu_{EHD} \approx 8.4 \times 10^{-7}$ m^2/V·s, about three times the hydronium ion mobility 2.9×10^{-7} m^2/V·s, and about six times the hydroxyl ion mobility ~1.3×10^{-7} m^2/V·s.

Bipolar Conduction

Many situations are best described by double injection. We extend the drift-dominated unipolar conduction model to two charge carriers of opposite signs with charge densities ρ_+ and ρ_- and respective mobilities μ_+ and μ_-, with recombination coefficient α and generation G within a dielectric of permittivity ϵ (37,38). The generation rate G increases with the number density of neutral molecules. Here we assume only weak dissociation so that the density of ionized carriers is much less than the density of neutrals. Under these conditions the generation rate G can be taken as constant in time and space. Similar bipolar conduction analysis has been used with electrostatic precipitators with back ionization, where ions are produced opposite in polarity to those produced at the discharge electrode. These "back corona" ions neutralize the charging ions by recombination, lower the electric field in the discharge region, lower the net charge acquired by the particles, and increase electric power consumption (39). Recent Kerr electro-optic field-mapping measurements in highly purified water have also shown systems with double injection which had an increase in breakdown strength with bipolar injection due to the decrease in electric field at both electrodes due to space charge shielding (15).

Governing Equations. Charge conservation for each carrier and Gauss's law for one-dimensional variations with the coordinate x yields

$$\frac{\partial J_+}{\partial x} + \frac{\partial \rho_+}{\partial t} = \alpha \rho_+ \rho_- + G \tag{78}$$

$$\frac{\partial J_-}{\partial x} + \frac{\partial \rho_-}{\partial t} = -\alpha \rho_+ \rho_- - G \tag{79}$$

$$\epsilon \frac{\partial E}{\partial x} = \rho_+ + \rho_- \tag{80}$$

where in the drift-dominated limit

$$J_+ = \rho_+ \mu_+ E, \quad J_- = -\rho_- \mu_- E \tag{81}$$

Equations (78) and (79) include charge recombination, when oppositely charged carriers overlap in space, and a constant generation due to thermal dissociation, which is field-independent. The recombination and generation terms cancel in equilibrium when the charge distributions are uniform in space and equal in magnitude but opposite in polarity, so that the net volume charge density everywhere is zero:

$$\rho_+ = -\rho_- = \rho_0 \Rightarrow G = \alpha \rho_0^2 \tag{82}$$

For our work, we assume Langevin recombination (40), where

$$\alpha = (\mu_+ + \mu_-)/\epsilon \tag{83}$$

This result is based on a simple model of electrostatic attraction of opposite charges. Langevin calculated the relative drift velocity between carriers and assumed that upon contact they neutralized each other.

The total terminal current per electrode unit area $J(t)$, given by the sum of conduction and displacement currents, is obtained by integrating over x between the electrodes with gap spacing ℓ the sum of the two charge conservation Eqs. (78) and (79):

$$(\rho_+ \mu_+ - \rho_- \mu_-) E + \epsilon \frac{\partial E}{\partial t} = J(t) = \frac{1}{\ell} \left[\epsilon \frac{dv}{dt} + \int_0^\ell (\rho_+ \mu_+ - \rho_- \mu_-) E \, dx \right] \tag{84}$$

Conductivity. The Ohmic conductivity is defined as

$$\sigma = \rho_+ \mu_+ - \rho_- \mu_- = \rho_0 (\mu_+ + \mu_-) \tag{85}$$

where the right-side equality assumes the thermal equilibrium of Eq. (82). Conductivity measurements are often made at low voltages, where the conditions of Eq. (82) are valid, so that the conductivity is essentially a constant in time and space. However, at high voltages, charge injection from the electrodes upsets equilibrium so that ρ_+ and ρ_- are not equal in magnitude everywhere and the effective conductivity varies with time and position.

The equilibrium charge density ρ_0 can be found from the equilibrium constant K of the dissociation reaction. For the case of highly purified water, the dissociation reaction is

$$H_2O \Rightarrow H^+ + OH^- \tag{86}$$

where in equilibrium the hydronium and hydroxyl products have equal concentrations given by

$$K_w = [H^+][OH^-] \Rightarrow [H^+] = [OH^-] = \sqrt{K_w} \tag{87}$$

The bracketed quantities are concentrations in moles/L. By multiplying these concentrations by Faraday's number, F = 96,488 C/mole, and converting liters to m^3 (1 liter = 10^{-3} m^3), the background equilibrium charge density of each ion $\pm\rho_0$ is

$$\rho_0 = 10^3 F \sqrt{K_w} \, C/m^3 \tag{88}$$

For the case of highly purified water at 24°C, $K_w = 10^{-7}$ moles/L (corresponding to pH = 7) so that ρ_0 = 9.65 C/m^3. This value is so high that even small imbalances in concentration between positive and negative charge carriers lead to a significant net charge that distorts the electric field distribution.

Method of Characteristics. The method of characteristics converts the hyperbolic partial differential equations (78)–(81) into a set of subsidiary ordinary differential equations, by rewriting Eqs. (78)–(81) in the frame of reference of each charge carrier moving at velocity

$$\frac{dx_+}{dt} = \mu_+ E, \quad \frac{dx_-}{dt} = -\mu_- E \tag{89}$$

The total time derivatives of the charge densities in each frame of reference is

$$\frac{d\rho_+}{dt} = \frac{\partial \rho_+}{\delta t} + \mu_+ E \frac{\partial \rho_+}{\partial x} = -\frac{\rho_+ \mu_+}{\epsilon}(\rho_+ + \rho_-) + \alpha \rho_+ \rho_- + G \quad \text{on } \frac{dx_+}{dt} = \mu_+ E \tag{90}$$

$$\frac{d\rho_-}{dt} = \frac{\partial \rho_-}{\delta t} - \mu_- E \frac{\partial \rho_-}{\partial x} = \frac{\rho_- \mu_-}{\epsilon}(\rho_+ + \rho_-) - \alpha \rho_+ \rho_- - G \quad \text{on } \frac{dx_-}{dt} = -\mu_- E \tag{91}$$

Similarly, using Eqs. (80) and (81) in Eq. (84) yields the electric field in each reference frame of the charge trajectories as

$$\frac{\partial E}{\partial t} + \mu_+ E \frac{\partial E}{\partial x} = \frac{dE}{dt} = \frac{\rho_- E}{\epsilon}(\mu_+ + \mu_-) + \frac{J(t)}{\epsilon} \text{ on } \frac{dx_+}{dt} = \mu_+ E \tag{92}$$

$$\frac{\partial E}{\partial t} - \mu_- E \frac{\partial E}{\partial x} = \frac{dE}{dt} = \frac{-\rho_+ E}{\epsilon}(\mu_+ + \mu_-) + \frac{J(t)}{\epsilon} \text{ on } \frac{dx_-}{dt} = -\mu_- E \tag{93}$$

Equations (89)–(93) are now in the standard form for Runge-Kutta numerical integration. All that is left to be supplied are the initial and boundary conditions.

A Simple Case Study of Bipolar Conduction. To illustrate the general approach with closed form solutions we consider the simple case where the positive carrier has zero mobility ($\mu_+ = 0$) and with no steady-state generation so that $G = 0$. Physically, we imagine some mechanism such as radiation instantaneously ionizing a region creating an equal number of positive and negative carriers uniformly distributed in space, each with charge density ρ_0. We assume that the lower electrode at $x = 0$ is at a positive voltage V with respect to the upper electrode at $x = \ell$. If the positive carriers are much larger than the negative carriers, their mobility is much less. In this zero mobility limit the positive charge carriers do not move ($dx_+/dt = 0$), while the negative carriers are swept toward the positive electrode and out of the system.

It is convenient to introduce the normalizations

$$\tilde{\rho}_\pm = \rho_\pm/\rho_0; \tilde{x} = x/\ell; \tilde{V} = \epsilon V/\rho_0 \ell^2$$
$$\tilde{\alpha} = \epsilon\alpha/\mu; \tilde{E} = \epsilon E/\rho_0 \ell; \tilde{t} = \rho_0 \mu_- t/\epsilon \tag{94}$$

ZERO RECOMBINATION LIMIT ($\alpha = 0$)

If the charges do not recombine ($\alpha = 0$) then the positive charge density in Eq. (90) with μ_+, α, and G equal to zero at every point remains constant with time ($\tilde{\rho}_+ = 1$). Because of the assumption of uniform ionization, this charge density is also constant in the region between the electrodes. The negative charge density can then be found by direct integration to yield

$$\tilde{\rho}_- = \frac{\tilde{\rho}_n}{[-\tilde{\rho}_n + (\tilde{\rho}_n + 1)\exp(\tilde{t}_0 - \tilde{t})]} \text{ on } \frac{d\tilde{x}}{d\tilde{t}} = -\tilde{E} \tag{95}$$

where $\tilde{\rho}_n$ is the negative charge density at the start of a characteristic trajectory at time $\tilde{t}_0$.

The characteristic trajectories of the negative charges are separated into two regions by the demarcation curve $\tilde{x}_d$ emanating from the position $\tilde{x} = 1$ at $\tilde{t} = 0$. The initial parameter $\tilde{\rho}_n$ is then zero ($\tilde{\rho}_n = 0$) along those characteristics which start at $\tilde{x} = 1$ for $\tilde{t}_0 > 0$ and $\tilde{\rho}_n = -1$ for those characteristics which emanate from the $\tilde{t} = 0$ boundary with $\tilde{x} = \tilde{x}_0$ and $\tilde{t}_0 = 0$. The negative charge density is then

$$\tilde{\rho}_n = \begin{cases} -1 & \tilde{t}_0 = 0 \quad \text{(Region I)} \\ 0 & \tilde{t}_0 > 0 \quad \text{(Region II)} \end{cases} \tag{96}$$

giving the total charge in each region as

$$\tilde{\rho}_T = \tilde{\rho}_+ + \tilde{\rho}_- = \begin{cases} 0 & \text{(Region I)} \\ 1 & \text{(Region II)} \end{cases} \tag{97}$$

This gives the electric field in each region as

$$\tilde{E} = \begin{cases} \tilde{E}_d & 0 \le \tilde{x} \le \tilde{x}_d \quad \text{(Region I)} \\ \tilde{E}_d + (\tilde{x} - \tilde{x}_d) & \tilde{x}_d \le \tilde{x} \le 1 \quad \text{(Region II)} \end{cases} \tag{98}$$

where $\tilde{x}_d$ is the position of the demarcation curve with $\tilde{E}_d$ the associated electric field, related as

$$\frac{d\tilde{x}_d}{d\tilde{t}} = -\tilde{E}_d \tag{99}$$

The applied voltage also requires the average electric field to be $\tilde{V}$ so that

$$\tilde{E}_d = \tilde{V} - \frac{1}{2}(1 - \tilde{x}_d)^2 \tag{100}$$

Using Eq. (100) in Eq. (99) gives the demarcation curve

$$\tilde{x}_d(\tilde{t}) = \begin{cases} 1 - \sqrt{2\tilde{V}}\tanh\left[\tilde{t}\sqrt{\tilde{V}/2}\right] & 0 \le \tilde{t} \le \tilde{t}_c \\ 0 & \tilde{t} \ge \tilde{t}_c \end{cases} \tag{101}$$

where $\tilde{t}_c$ is the time when the demarcation curve reaches the $\tilde{x} = 0$ boundary so that all the negative charge has been swept out of the system. This only happens in a finite time if $\tilde{V} > 0.5$. For $\tilde{V} = 0.5$, $\tilde{t}_c = \infty$ while if $\tilde{V} < 0.5$, $\tilde{x}_d$ never reaches zero but rather approaches the steady-state value $1 - \sqrt{2\tilde{V}}$ so that the negative charge never completely leaves the system. Once the demarcation curve is known, all other trajectories obey the relation

$$\tilde{x}(\tilde{t}) = \begin{cases} \tilde{x}_0 + \tilde{x}_d(\tilde{t}) - 1 & \text{(Region I)} \\ \tilde{x}_d(\tilde{t}) + [1 - \tilde{x}_d(\tilde{t}_0)]\exp(\tilde{t}_0 - \tilde{t}) & \text{(Region II)} \end{cases} \tag{102}$$

where the parameter $\tilde{x}_0$ is the starting position at $\tilde{t} = 0$ for characteristic curves in Region I, and $\tilde{t}_0$ is the starting time at $\tilde{x} = 1$ for characteristic curves in Region II. The demarcation curve is obtained again for $\tilde{x}_0 = 1$ and $\tilde{t}_0 = 0$.

The electric field along these curves is

$$\tilde{E}(\tilde{t}) = \begin{cases} \tilde{V} - \frac{1}{2}[1 - \tilde{x}_d(\tilde{t})]^2 & \text{(Region I)} \\ \tilde{x} + \tilde{V} - \frac{1}{2}\{1 + [\tilde{x}_d(\tilde{t})]^2\} & \text{(Region II)} \end{cases} \tag{103}$$

Figure 12 shows the results for voltages $\tilde{V} = 1.0$, $\tilde{V} = 0.5$, and $\tilde{V} = 0.25$.

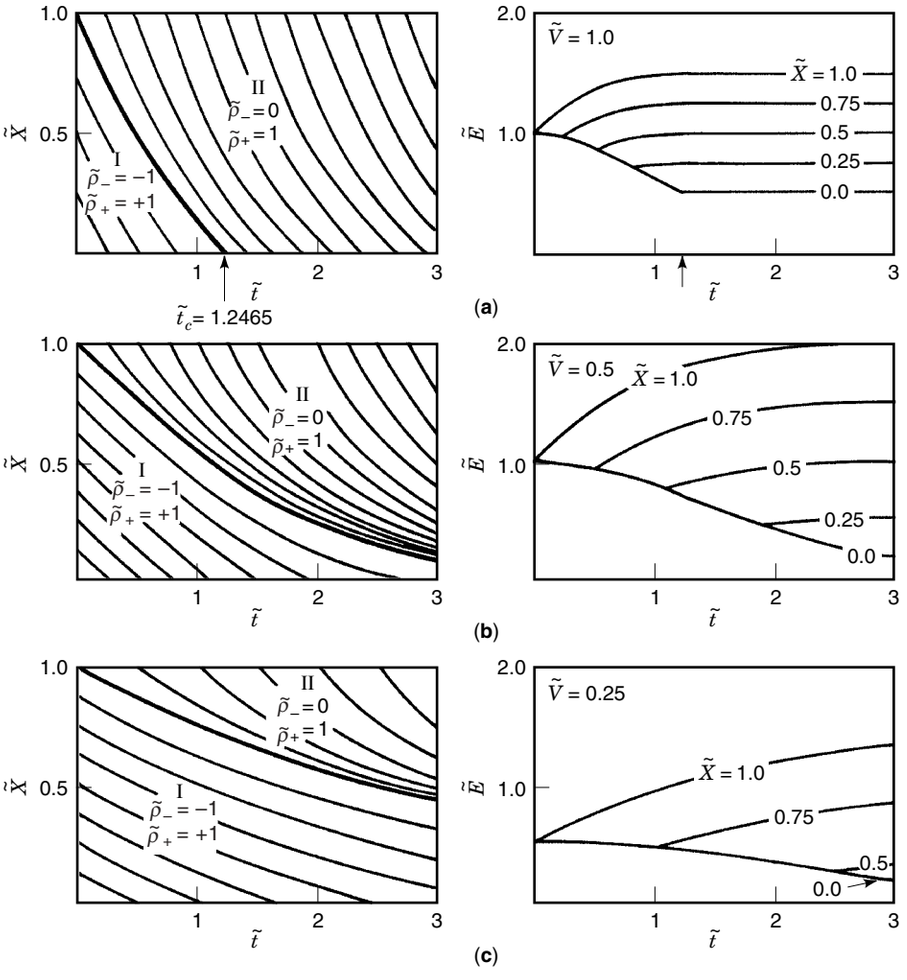

Figure 12. Characteristic trajectories and time dependence of the electric field at various positions for an immobile positive charge ($\mu_+ = 0$) with no recombination ($\alpha = 0$) or generation ($G = 0$): (a) $\tilde{V} = 1.0$, (b) $\tilde{V} = 0.5$, and (c) $\tilde{V} = 0.25$.

The terminal current per unit electrode area is found from Eq. (84) as

$$\tilde{J} = \tilde{V} - \frac{1}{2}[\tilde{E}^2(1,\tilde{t}) - \tilde{E}^2(0,\tilde{t})]; \quad \tilde{J} = \epsilon J/(\mu_- \rho_0^2 \ell) \tag{104}$$

and is plotted in Fig. 13 for various voltages.

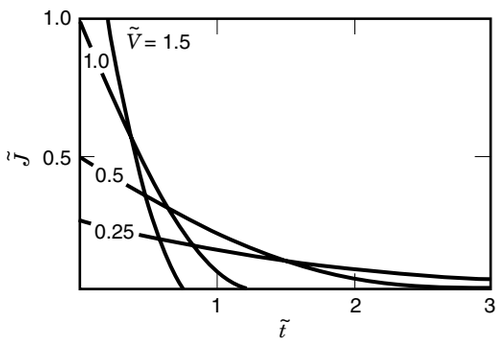

Figure 13. Terminal current per unit electrode area for various values of applied voltage.

LANGEVIN RECOMBINATION LIMIT

In our zero mobility limit for the positive charge the normalized Langevin recombination coefficient of Eqs. (83) and (94) is unity ($\tilde{\alpha} = 1$). In this limit, the equation for $\tilde{\rho}_-$ is independent of $\tilde{\rho}_+$ with solutions along the trajectories of the negative charge

$$\tilde{\rho}_- = \frac{\tilde{\rho}_n}{[1 - \tilde{\rho}_n(\tilde{t} - \tilde{t}_0)]} \text{ along } \frac{d\tilde{x}}{d\tilde{t}} = -\tilde{E} \tag{105}$$

where again $\tilde{\rho}_n$ is the negative charge density at $\tilde{t}_0$ given in Eq. (96). We again define regions separated by the dark demarcation curves $\tilde{x}_d$ in Fig. 14(a) emanating from $\tilde{x} = 1$, drawn for various voltages. In Region II above the demarcation curve, $\tilde{\rho}_n = 0$ so that the negative charge density is zero everywhere in this region. In Region I, $\tilde{\rho}_n = -1$ with $\tilde{t}_0 = 0$ so that the negative charge density of Eq. (105) is

$$\tilde{\rho}_- = \begin{cases} -\dfrac{1}{1+\tilde{t}} & \tilde{t}_0 = 0 \quad \text{(Region I)} \\ 0 & \tilde{t}_0 > 0 \quad \text{(Region II)} \end{cases} \tag{106}$$

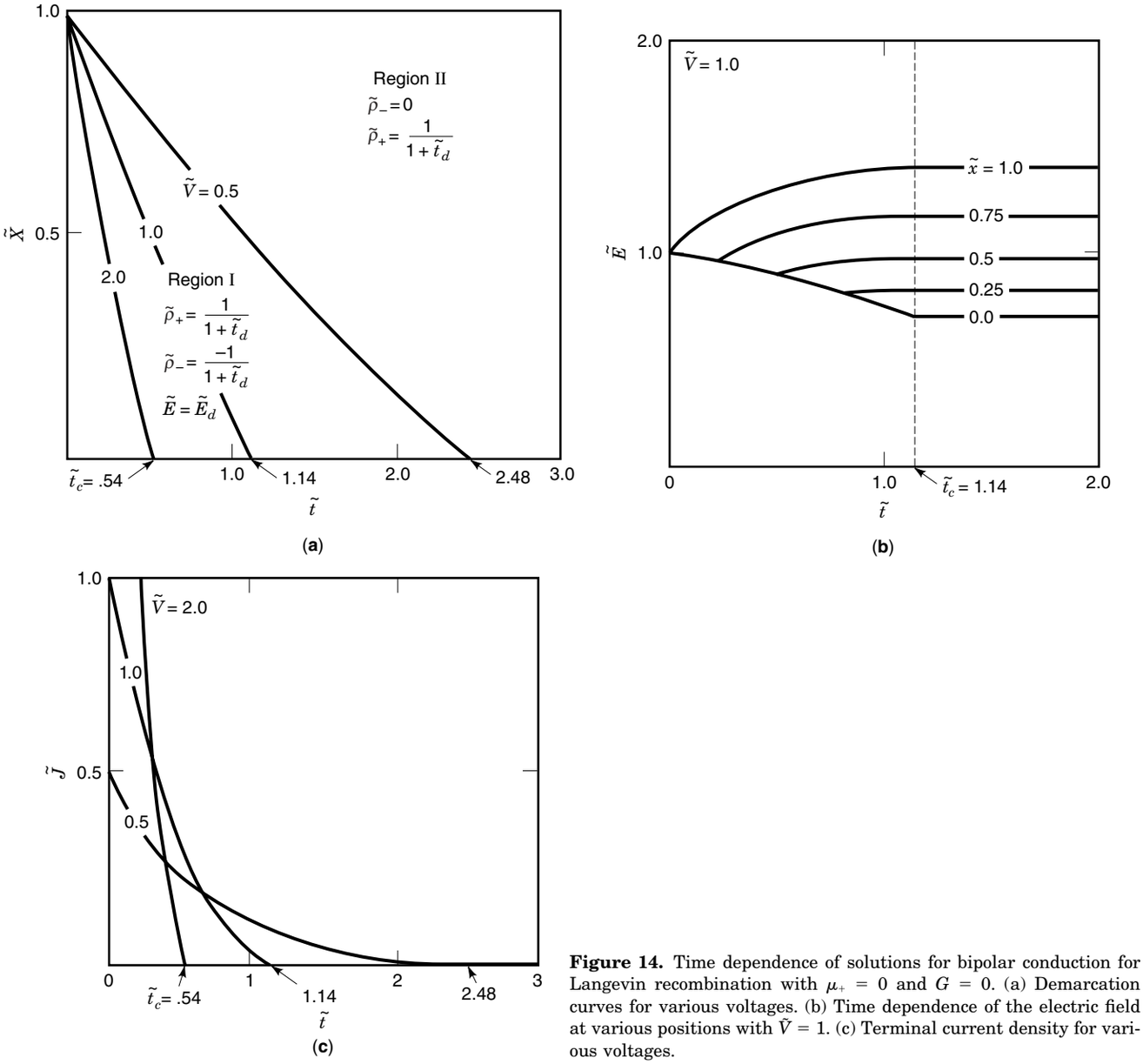

Figure 14. Time dependence of solutions for bipolar conduction for Langevin recombination with $\mu_+ = 0$ and $G = 0$. (a) Demarcation curves for various voltages. (b) Time dependence of the electric field at various positions with $\tilde{V} = 1$. (c) Terminal current density for various voltages.

The positive charge along its stationary trajectories $d\tilde{x}/d\tilde{t} = 0$, represented by the dashed straight lines in Fig. 14(a), can now be found by direct integration of Eq. (90) with $\tilde{\alpha} = 1$, $\mu_+ = 0$, and $\tilde{G} = 0$ since $\tilde{\rho}_-$ is known from Eq. (106)

$$\tilde{\rho}_+ = \begin{cases} \dfrac{1}{1+\tilde{t}} & \text{(Region I)} \\ \dfrac{1}{1+\tilde{t}_d} & \text{(Region II)} \end{cases} \tag{107}$$

where $\tilde{t}_d$ is the time the straight line positive charge trajectories intersect the demarcation curve at position $\tilde{x}_d$. Once in Region II the positive charge density at a particular position remains constant as there is no longer any negative charge to recombine with.

All variables can be expressed in terms of the time dependence of the position $\tilde{x}_d$ and associated negative field $\tilde{E}_d$ along the demarcation curve separating regions. The terminal current is

$$\tilde{J}(\tilde{t}) = -\int_0^{\tilde{x}_d} \tilde{\rho}_- \tilde{E} d\tilde{x} = \frac{\tilde{E}_d \tilde{x}_d}{1+\tilde{t}} \tag{108}$$

where we use the fact that the net charge in Region I is zero so that the electric field at a given time does not depend on position and is equal to the electric field $\tilde{E}_d$.

The electric field along the demarcation curve then obeys the relation

$$\frac{d\tilde{E}_d}{d\tilde{t}} = \tilde{J}(\tilde{t}) - \tilde{\rho}_+ \tilde{E}_d = \frac{\tilde{E}_d}{1+\tilde{t}}(\tilde{x}_d - 1) \tag{109}$$

which can be rewritten as

$$\frac{d}{d\tilde{t}}[\tilde{E}_d(1+\tilde{t})] = \tilde{E}_d\tilde{x}_d \tag{110}$$

Since

$$\frac{d\tilde{x}_d}{d\tilde{t}} = -\tilde{E}_d \tag{111}$$

Eqs. (110) and (111) can be directly integrated to yield

$$\begin{aligned}\tilde{E}_d &= \frac{a^2-\tilde{x}_d^2}{2(1+\tilde{t})}; a^2 = 2\tilde{V}+1\\ \tilde{x}_d &= a\frac{[a+1-(a-1)(1+\tilde{t})^a]}{[a+1+(a-1)(1+\tilde{t})^a]}\end{aligned} \tag{112}$$

where we used the initial conditions

$$\tilde{x}_d(\tilde{t}=0) = 1,\ \tilde{E}_d(\tilde{t}=0) = \tilde{V} \tag{113}$$

Without loss of generality we assume $\tilde{V}$ to be positive so that the electric field is positive and the negative charges are swept toward the lower positive electrode.

1. Zero Voltage ($\tilde{V} = 0$). If there is no applied voltage, the parameter "a" becomes unity and the positive and negative charges do not separate but remain stationary and recombine. In this limit there is only Region I with the demarcation curve described by

$$\tilde{x}_d = 1,\ \tilde{E}_d = 0 \tag{114}$$

so that the electric field and terminal current remain zero for all time. Each charge decays due to recombination as

$$\tilde{\rho}_+ = -\tilde{\rho}_- = \frac{1}{1+\tilde{t}} \tag{115}$$

2. Positive Voltage ($\tilde{V} > 0$). For a finite positive voltage, Region I extends over the interval until $\tilde{x}_d = 0$ which occurs at the time $\tilde{t}_c$

$$\tilde{t}_c = \left(\frac{a+1}{a-1}\right)^{1/a} - 1 \tag{116}$$

After this time ($\tilde{t} \geq \tilde{t}_c$), the system is in the steady state with $\tilde{J}(\tilde{t}) = 0$. Figure 14(b) plots the time dependence of the electric field at various positions for $\tilde{V} = 1$ while Fig. 14(c) shows the terminal current per unit electrode area according to Eq. (108) for various values of $\tilde{V}$.

The charge density in Region II at constant $\tilde{x}$ remains constant with time as given by Eqs. (106) and (107). We can find how the charge varies with position at a fixed time by solving Eq. (112) for $(1 + \tilde{t})$ in terms of $\tilde{x}_d$

$$(1+\tilde{t}) = \left[\frac{(\tilde{x}_d-a)(1+a)}{(\tilde{x}_d+a)(1-a)}\right]^{1/a} \tag{117}$$

We then find the electric field from Gauss's law by integrating

$$\frac{\partial\tilde{E}}{\partial\tilde{x}} = \tilde{\rho}_+ + \tilde{\rho}_- = \left[\frac{(\tilde{x}+a)(1-a)}{(\tilde{x}-a)(1+a)}\right]^{1/a} \tag{118}$$

This relation can be integrated in terms of hypergeometric functions. For $\tilde{t} \geq \tilde{t}_c$ the system is in the dc steady state.

KERR ELECTROOPTIC FIELD MAPPING MEASUREMENTS

Measuring the electric field is useful in the study and modeling of high voltage conduction and breakdown characteristics in insulating liquids since the conduction laws are often unknown and the electric field cannot be found from the geometry alone by solving the Poisson equation with unknown volume and surface charge distributions. Optical measurement of high electric fields offers near-perfect electrical isolation between the measured field and the measuring instrumentation, avoids interference errors, and makes extensive shielding and insulation requirements unnecessary (41).

Governing Electrooptic Equations

High-voltage stressed liquids are usually birefringent, in which case the refractive indices for light (of free-space wavelength λ) polarized parallel $n_\parallel$ and perpendicular $n_\perp$ to the local electric field are related by

$$n_\parallel - n_\perp = \lambda B E^2 \tag{119}$$

where B is the Kerr constant and E is the magnitude of the applied electric field (42). The phase shift ϕ between light-field components propagating in the direction perpendicular to the plane of the applied electric field along an electrode length L is

$$\phi = 2\pi B E^2 L = \pi(E/E_m)^2, E_m = (2BL)^{-1/2} \tag{120}$$

If the birefringent dielectric is placed within a circular polariscope with aligned or crossed polarizers, the transmitted light intensity is

$$\frac{I}{I_0} = \begin{cases}\sin^2\dfrac{1}{2}\pi(E/E_m)^2, \text{ crossed polarizers (CP)}\\ \cos^2\dfrac{1}{2}\pi(E/E_m)^2, \text{ aligned polarizers (AP)}\end{cases} \tag{121}$$

Light minima and maxima occur when

$$\frac{E}{E_m} = \sqrt{n}\begin{cases} n \text{ odd} \begin{pmatrix}\text{minima AP}\\ \text{maxima CP}\end{pmatrix}\\ n \text{ even} \begin{pmatrix}\text{minima CP}\\ \text{maxima AP}\end{pmatrix}\end{cases} \tag{122}$$

E_m is thus the field magnitude for first maximum with crossed polarizers and first minimum with aligned polarizers. For test cells of length $L = 1.1$ m with highly purified water at $\lambda = 590$ nm, $B \approx 2.8 \times 10^{-14}$ m/V^2, and $E_m \approx 35 - 36$ kV/cm. As an example of Kerr measurements of electric field distributions, Fig. 15 shows a circular polariscope experimental apparatus with a representative measurement using coaxial cylindrical electrodes.

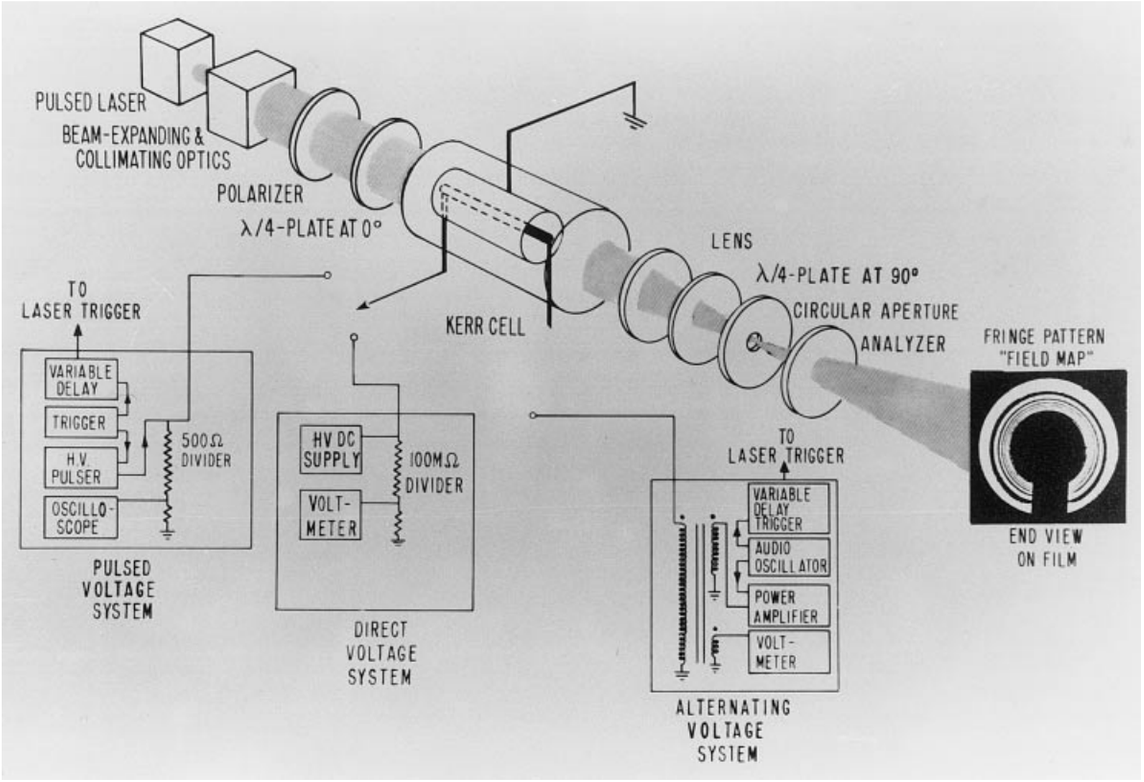

Figure 15. Circular polariscope experimental configuration shown for Kerr electrooptic field-mapping measurements using coaxial cylindrical electrodes for pulsed, dc, and ac high voltages. The photographic film shows circular light minima and maxima as the nonuniform electric field between cylindrical electrodes satisfies the conditions of Eq. (122) for multiple values of n.

When a high-voltage pulse is applied, as in Fig. 16, a photodetector records a series of maxima and minima related by $\sqrt{n}$ as in Eq. (122).

Visualization of Space-Charge Distortion of the Electric Field

The patterns of light minima and maxima described by Eqs. (121) and (122) allow direct visualization of how the electric field distribution becomes distorted due to space charge. Figure 17 shows representative Kerr effect optical patterns of the electric field distribution in ethylene carbonate [$C_3H_4O_3$], a high Kerr constant liquid above 36°C with $B \approx 2 \times 10^{-12}$ m/V^2, at various times after a high-voltage pulse is applied to parallel plate electrodes. This Kerr constant is almost as large as that of nitrobenzene, which has a Kerr constant $B \approx 3 \times 10^{-12}$ m/V^2, but without the toxicity of nitrobenzene. At time near zero, the uniform light intensity in the central interelectrode region indicates the space-charge free electric field as there has not been sufficient time for charge to migrate from the electrodes into the dielectric volume. The side lines outside the interelectrode region are due to the fringing electric field decaying to zero with increasing distance from the electrodes. As time increases, positive space charge migrates into the interelectrode dielectric region causing a highly nonuniform electric field with a small field near the positive electrode and a large field at the negative electrode corresponding to positive charge injection with maximum charge density of order 1 C/m^3.

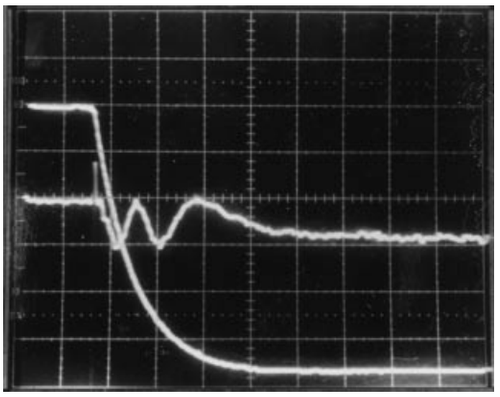

Figure 16. The output of an optical photomultiplier tube goes through a series of minima and maxima [here, $n = 1 - 4$ in Eq. (81)] when a 100 kV negative high-voltage pulse is applied to parallel plate electrodes of 1.1 m length and 1 cm gap shown here for 77% water, 23% ethylene glycol by weight at 2.7°C using crossed polarizers (time base 20 μs cm^{-1}). From this measurement, the Kerr constant of the mixture at $\lambda = 633$ nm wavelength is $B \approx 2.2 \times 10^{-14}$ m/V^2 with $E_m \approx 45.6$ kV/cm.

Figure 17. Kerr electrooptic fringe patterns in ethylene carbonate at T = 42.9°C with resistivity ~4 MΩ-cm at early (~20 μs) and long times (1, 2, 3 and 4 ms) after charging from a Marx generator at 60 kV with stainless steel electrodes of length 35 cm and gap of 1 cm. At early time (~20 μs), the uniform light intensity in the central interelectrode region indicates the space-charge free uniform electric field, while the interelectrode fringes at longer times indicate significant positive charge injection. The 60 kV charging voltage is given in the upper right, while the instantaneous voltage is given at the lower right of each photograph. $E_m \approx 8.3$ kV/cm.

Figure 18 shows uniform positive charge injection of ~0.09 C/m^3 in nitrobenzene for a dc high voltage including significant field enhancement behind the cathode as well as the same test cell excited with 60 Hz ac high voltage (43). The dc electric field at the cathode is $E \approx 41.6$ kV/cm while at the anode $E \approx 31.0$ kV/cm. The optical pattern shown at the peak of the 60 Hz cycle corresponds to homopolar charge injection with linearly varying charge density from ~−0.18 C/m^3 at the cathode to +0.18 C/m^3 at the anode. The maximum electric field at the center is ~44.9 kV/cm while the electric fields at the electrodes are ~39.2 kV/cm.

Figure 19 shows the optical patterns at various times in an ac 60 Hz cycle with period $T \approx 16.67$ ms. In particular, at time 1/2 T the applied sinusoidal voltage is instantaneously zero yet light appears near the electrodes. This is due to the electric field of ~±9 kV/cm at each electrode caused by a uniform charge distribution ~0.1 C/m^3 that does not vary with time.

The dynamics of charge injection and transport from electrodes for homocharge bipolar conduction in nitrobenzene can be seen in Fig. 20. When stressed by a 30 kV step high voltage with ~1 μs risetime applied to stainless steel parallel plate electrodes with 1 cm spacing and length L =10 cm, Fig. 20 shows selected frames taken from a high-speed movie at ~5000 frames/s of Kerr electrooptic field mapping measurements using crossed polarizers, where $E_m \cong 12$ kV/cm. At

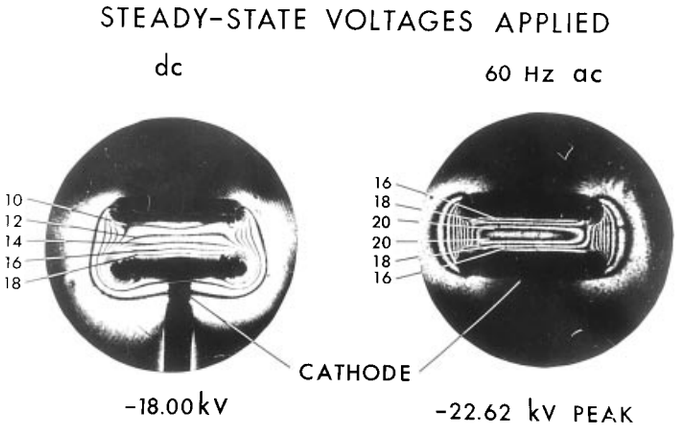

Figure 18. Typical observations of the fringe patterns resulting from the application of direct and 60 Hz, 16 kV rms alternating high voltages in nitrobenzene with parallel plate electrodes of length 12 cm and 0.5 cm gap. The interelectrode fringes show that the interelectrode field is not uniform under these conditions. $E_m \approx 9.8$ kV/cm.

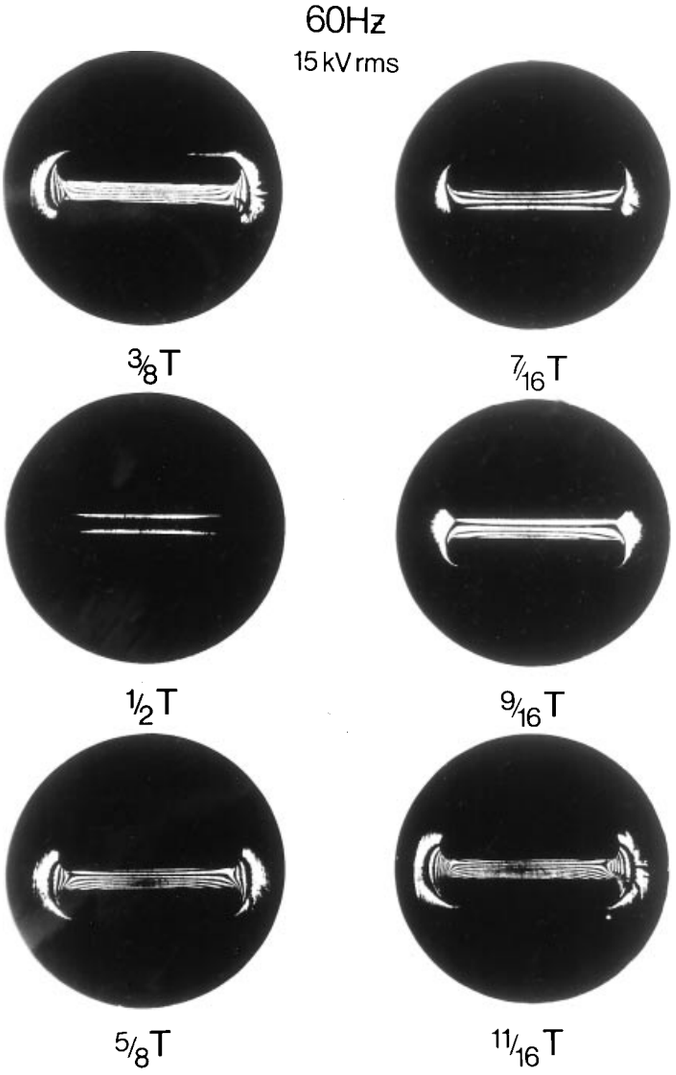

Figure 19. Kerr electrooptic fringes with crossed polarizers in nitrobenzene over the course of a 60 Hz, 15 kV rms high-voltage waveform. The significant light transmission at 1/2 T when the voltage is instantaneously zero indicates significant volume charge. $E_m \approx 9.2$ kV/cm.

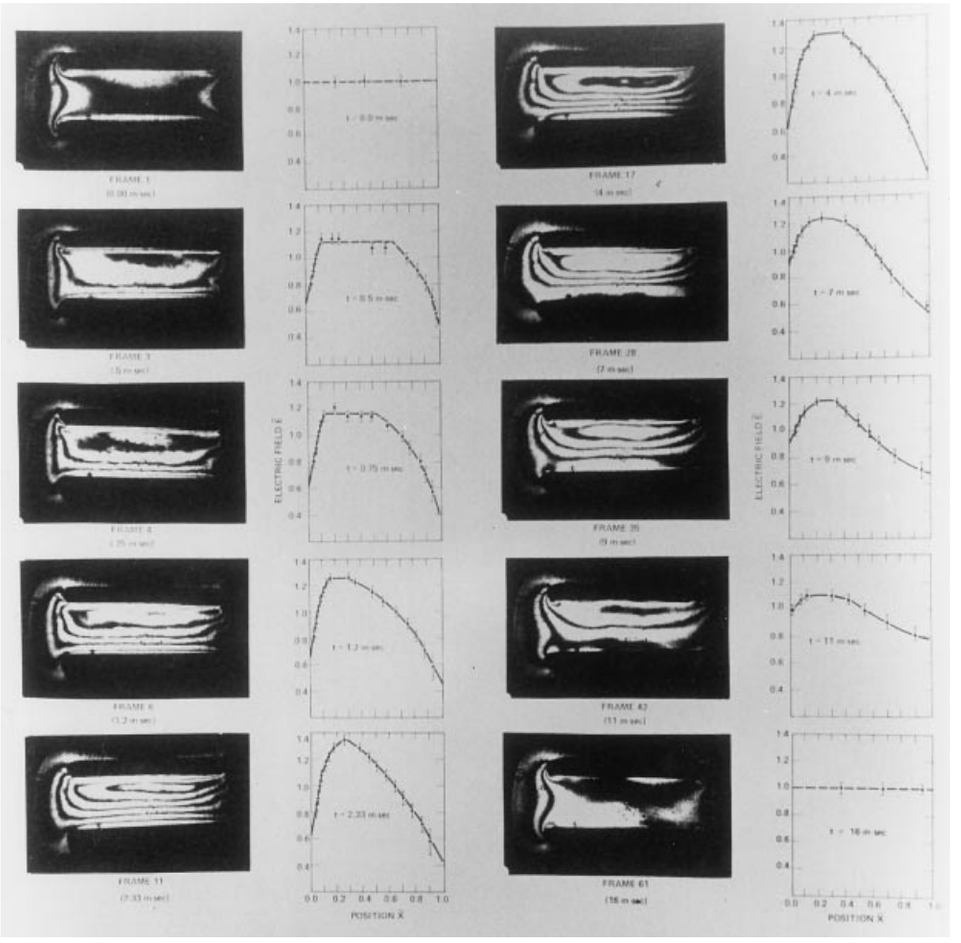

Figure 20. Transient Kerr electrooptic field mapping measurements at ~5000 frames/s with crossed polarizers in nitrobenzene ($E_m \approx 12$ kV/cm) showing bipolar conduction when a stepped 30 kV high voltage is applied across parallel plate electrodes of length 10 cm with a 1 cm gap. To the right of each photograph is a plot of $\tilde{E} = Ed/V$ vs $\tilde{x} = x/d$ where x is measured from the upper positive electrode. Data points are shown for each light transmission maxima and minima. The space-charge density is proportional to the slope of the electric field distribution; thus we have positive charge injected from the upper ($\tilde{x} = 0$) positive electrode and negative charge injected from the lower ($\tilde{x} = 1$) negative electrode. The negative charge moves about four times faster than the positive charge.

$t = 0$ and for $t > 16$ ms, the field is essentially uniform, evidenced by the lack of fringes indicating no net charge density. However, the bipolar conduction process is shown during the transient interval by the propagation of fringe lines from the positive and negative electrodes. The field distributions also plotted in Fig. 20 have a slowly propagating positive slope near the positive electrode, indicating positive space charge; and a faster moving negative slope near the negative electrode indicating more mobile negative space charge. At about $t = 2.33$ ms, the two charge fronts meet and the charges recombine to a charge-neutral steady state. The approximate mobilities for positive and negative charge carriers in nitrobenzene are $\mu_+ \approx 0.7 \times 10^{-6}$ m^2/(V = s) and $\mu_- \approx 2.8 \times 10^{-6}$ m^2/(V = s).

Coaxial Cylindrical Electrodes

Space-charge shielding can also cause a stress inversion in nonuniform field electrode geometries for coaxial cylindrical electrodes. The dc steady-state electric field distributions shown in Fig. 21 are found by solving the unipolar ion conduction equations of Eqs. (53)–(55) in cylindrical geometry (44,45). In the absence of space charge we have the usual maximum field at the inner cylinder of radius R_i decreasing as $1/r$ to the outer cylinder of radius R_0. With unipolar injection from the inner cylinder, the field drops at the inner cylinder and increases at the outer cylinder; the area under the electric field curve remains constant at the applied voltage V. When the electric field E_i at the inner cylinder drops to $E_i R_o/V = (1 - R_1/R_o)$, the electric field is constant across the gap. Any further lowering of the electric field at the inner cylinder results in a stress inversion as the electric field is least at the inner cylinder and increases to the outer cylinder. This occurs when the injected charge is so large that the space-charge shielding reduces the electric field due to the sharp geometry. If the unipolar injection is from the outer cylinder, the field drops at the outer cylinder and further in-

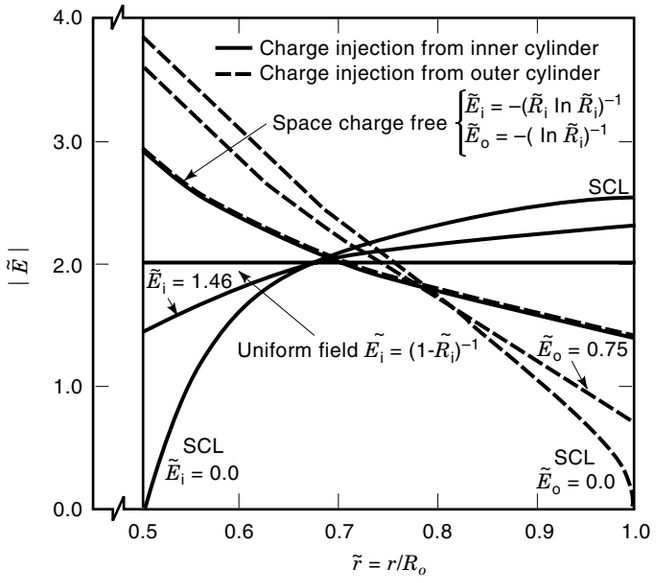

Figure 21. Theoretical electric field magnitude distributions $|\tilde{E}| = |ER_0/V|$ for unipolar drift-dominated conduction between coaxial cylindrical electrodes at voltage V with inner radius $\tilde{R}_i = R_i/R_0 = 0.5$ with positive charge injection from the inner cylinder (solid lines) or outer cylinder (dashed lines) for various values of emitter electric fields $\tilde{E}_i = E(r = R_i)R_o/V$ or $\tilde{E}_o = E(r = R_o)R_o/V$. Space-charge limited (SCL) injection has $\tilde{E}_i = E(r = R_i) = 0$ at $r = R_i$ or $\tilde{E}_o = E(r = R_o) = 0$ at $r = R_o$.

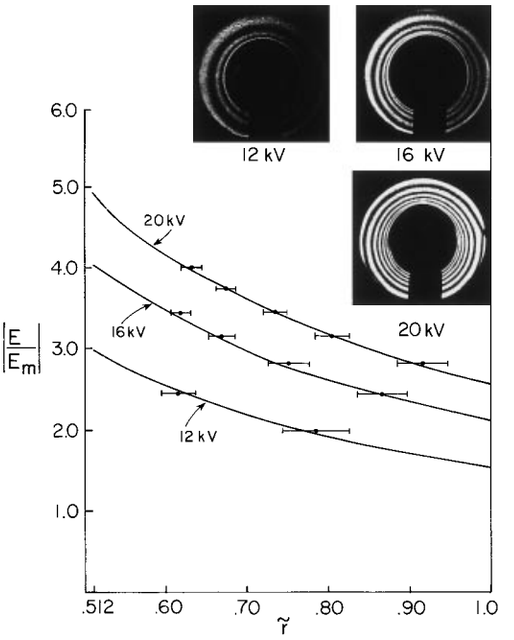

Figure 22. Electric field space-charge free $1/r$ distributions between coaxial cylindrical electrodes with inner radius of 0.512 cm and outer radius 1 cm, and length 10 cm together with associated Kerr patterns for various 100 μs duration pulsed voltages; $E_m \approx 9.8$ kV/cm.

creases the field at the inner cylinder. Figure 22 shows the theoretical $1/r$ space-charge free fields and associated Kerr fringe patterns for various 100 μs pulsed high voltages in nitrobenzene (46). Figure 23 shows Kerr electrooptic field mapping measurements in highly purified nitrobenzene with unipolar positive injection with dc high voltages. When the inner cylinder is positive, the electric field drops at the outer cylinder and increases at the inner cylinder. For less purified nitrobenzene, Fig. 24 shows that the greater conductivity causes an increase in charge injection so that there is a stress inversion with the field least at the positive-charge injecting inner cylinder.

Figure 25 shows Kerr effect measurements over the course of a sinusoidal voltage cycle. The left half of the photographs in Fig. 25 shows the half-cycle where the outer cylinder is positive and the field distribution corresponds closely to the $1/r$ charge-free case. The right half of the photographs in Fig. 25 show the half-cycle where the inner cylinder is positive. The electric field is highly uniform due to significant positive charge injection. Such asymmetrical nonlinear behavior over the course of a sinusoidal cycle leads to harmonic generation.

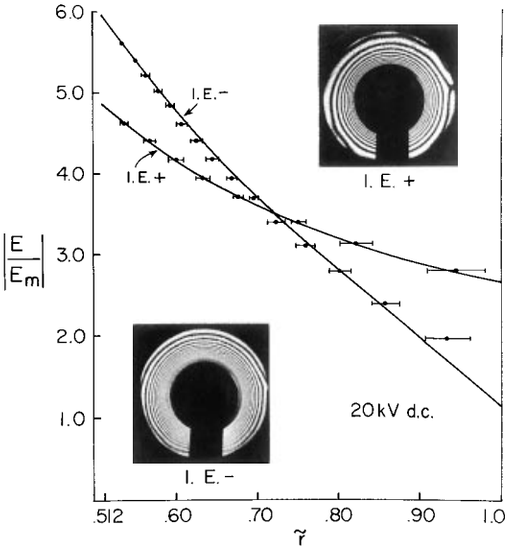

Figure 23. Dc electric field distributions with Kerr effect data ($E_m \approx 9.8$ kV/cm) showing effects of polarity reversal with inner electrode positive (I.E.+) and inner electrode negative (I.E.−) at 20 kV with highly purified nitrobenzene. Stainless steel cylindrical electrodes have inner radius 0.512 cm and outer radius 1 cm with length 10 cm. The solid lines are obtained from unipolar analysis with a best fit to the data chosen for the electric field at the positive electrode. Note that the weaker electric field regions, evidenced by broader, less densely spaced fringes, are near the outer cylinder. For both polarities increasing the voltage across the cylinders causes the fringes to move outward and disappear into the outer cylinder.

Representative Measurements in Highly Purified Water

Representative pulsed high-voltage measurements of highly purified water are shown in Fig. 26 with parallel plate electrodes for different metallic electrodes showing differences in the magnitude and sign of the injected charge (15). Stainless steel electrodes generally inject positive charge, aluminum injects negative charge, while brass can inject either positive or negative charge. Thus by appropriate choice of electrode material combinations and voltage polarity, it is possible to

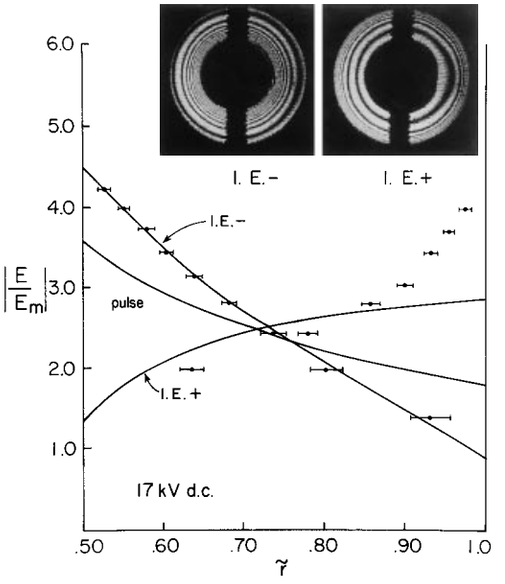

Figure 24. Electric field distributions with Kerr effect data ($E_m \approx$ 11.5 kV/cm) showing effects of polarity reversal with inner electrode positive (I.E.+) and inner electrode negative (I.E.−) at 17 kV with less purified nitrobenzene. Stainless steel cylindrical electrodes have inner radius 0.5 cm and outer radius 1 cm with length 8.5 cm. The solid lines are obtained from unipolar analysis with a best fit to the data chosen for the electric field at the positive electrode. Note that when the inner cylinder is positive (I.E.+), the region of weaker field strength is near the inner cylinder so that increasing the voltage across the cylinders causes the fringes to collapse upon the inner cylinder. There is a poor fit between unipolar theory and measurement when the inner electrode is negative (I.E.−), where the fringes move outward as the voltage is increased.

have uncharged, unipolar charged negative or positive, or bipolar homocharge charged liquid.

Breakdown strengths are generally higher with bipolar injection. For example, with brass-aluminum electrodes, the polarity for bipolar injection had a breakdown strength of ~125 to 135 kV/cm, while the reverse polarity had negative charge injection with breakdown strength ~90 to 95 kV/cm. Similarly, stainless steel-aluminum electrodes had a breakdown strength with bipolar injection of ~125 to 140 kV/cm, while the reverse polarity had no charge injection with a breakdown strength of ~105 kV/cm. This increase in breakdown strength for homocharge distributions is due to the decrease in electric field at both electrodes due to the space-charge shielding as shown in Fig. 10(c). The electric field is increased in the center of the gap, but breakdown does not occur because the intrinsic strength of the dielectric in the volume is larger than at an interface.

The positive space-charge injection from a pair of parallel-plate stainless steel electrodes as a function of time is shown in Fig. 27. At early times, $t < 250$ μs, the interelectrode light intensity distribution is uniform, indicating a uniform electric field. At $t \sim 500$ μs, numerous dark fringes appear near the positive electrode. The light distribution is uniform in front of the fringes with the electric field decreasing back to the positive electrode. A weak field near the positive electrode and stronger field near the negative electrode from Fig. 10(b) indicates a net positive space-charge distribution near the positive electrode with zero space charge in the uniform field region. At later times, the charge front moves toward the negative electrode. The electric field distribution is plotted for various times in Fig. 28.

Note in Fig. 27 that the terminal voltage v listed at the lower right of each photograph decays with time after it has reached crest. In the time interval 0 to 500 μs, the nondimensional electric field El/v at the $x/l = 0$ electrode (anode) drops from 1.0 to ~0.4, while at the opposite $x/l = 1$ electrode (cathode), the nondimensional field rises from 1.0 to >1.1. For later times, the injection field at $x = 0$ remains almost constant at $El/v \sim 0.5$, while the electric field at $x/l = 1$ increases smoothly to greater than 1.3. As a check, for all times the area under the nondimensional electric field curves must be unity. Near $x = 0$, the slope is about three. Using representative values of $v = 100$ kV, $\epsilon = 80\epsilon_0$, and gap $l = 1$ cm, the dimensional charge density is then $q \cong 2$ C/m^3.

To obtain a feel of the size of q, we can compare this net charge density to the background charge density of the water dissociation products of hydronium (H_3O^+) and hydroxyl

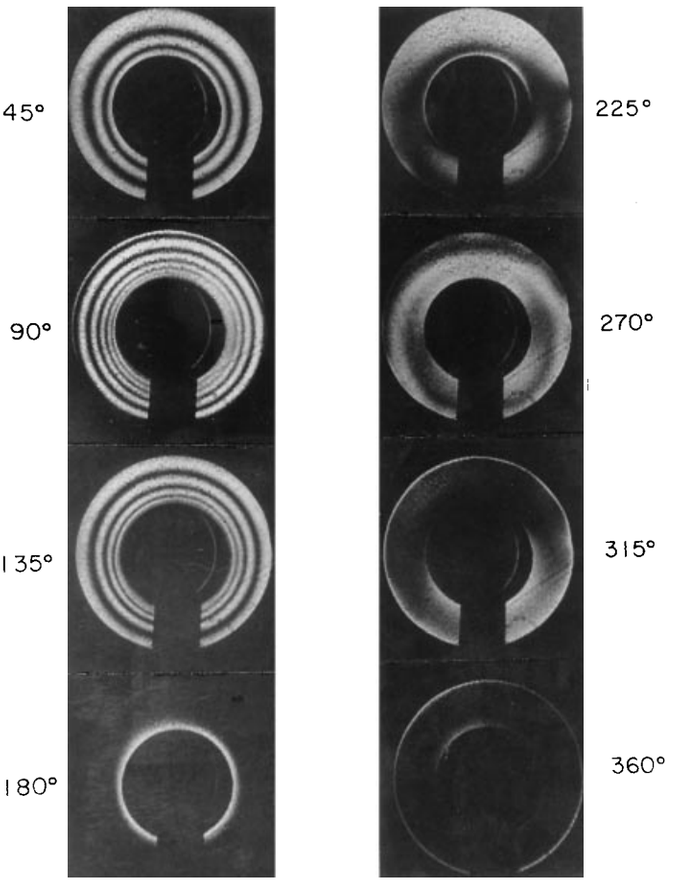

Figure 25. Kerr effect data ($E_m \approx$ 9.8 kV/cm) taken over the course of a 40 Hz, 14 kV peak sinusoidal voltage using the cylindrical electrodes described in Fig. 23. From 0° to 180° the inner cylinder is negative with very little charge injection, while from 180° to 360° the inner cylinder is positive with significant charge injection causing an essentially uniform electric field as evidenced by the lack of fringes.

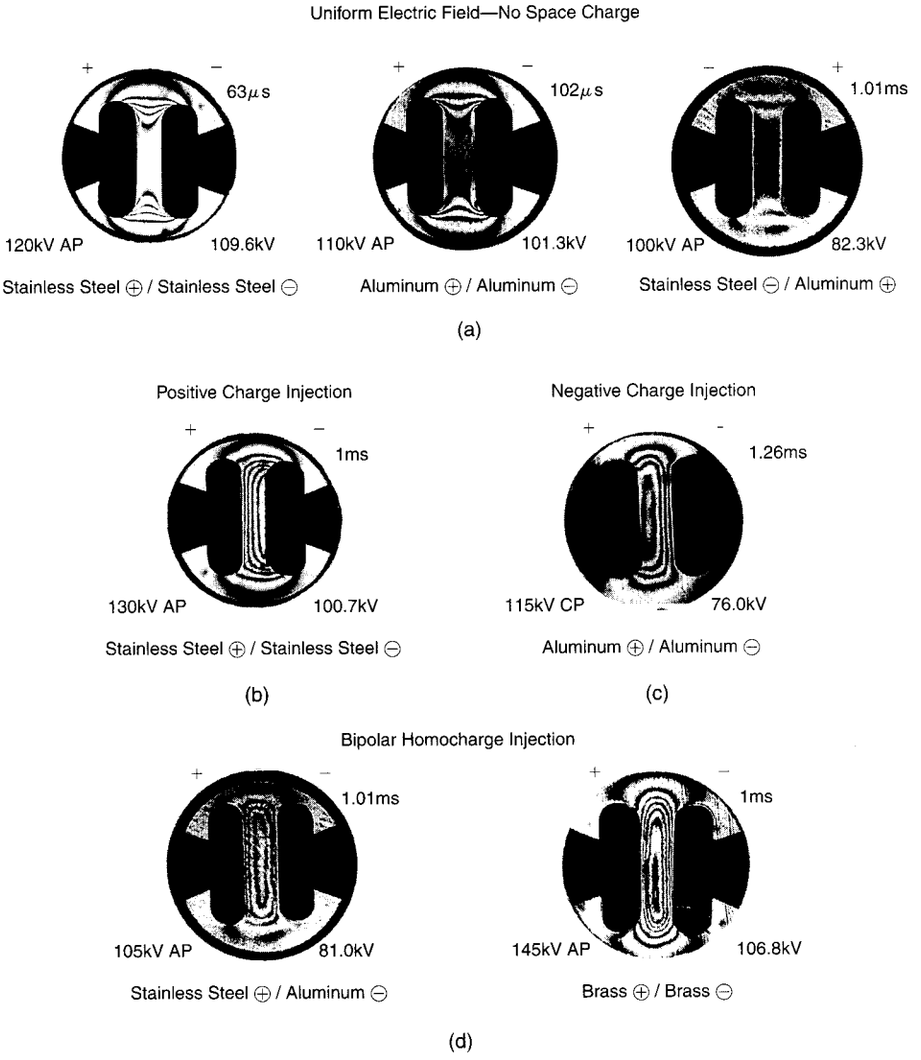

Figure 26. Representative Kerr effect measurements with a 1 cm gap between 1.1 m long parallel-plate electrodes stressed by a high-voltage step in highly purified water with $E_m \approx 35 - 36$ kV/cm; (a) the space-charge-free uniform electric field distribution so that the Kerr effect shows uniform light transmission in the interelectrode gap region. At times less than about 100 μs after the step was applied, the dielectric is essentially space-charge free for all electrode metal combinations. With stainless steel negative and aluminum positive, the dielectric is space-charge free for all time; (b) positive charge injection with stainless steel electrodes so that the electric field distribution has positive slope with decreased electric field near the positive electrode and increased field at the negative electrode; (c) negative charge injection with aluminum electrodes so that the electric field distribution has negative slope with decreased electric field near the negative electrode and increased field at the positive electrode; (d) bipolar homocharge injection, where the electric field is decreased at both charge-injecting electrodes, with the peak field in the central gap region. In each photograph, the electrode metals and polarity are listed at the bottom; the initial charging voltage and whether aligned (AP) or crossed (CP) polarizers are used are given at the lower left; the instantaneous voltage is given at the lower right; and the time after high voltage is applied is given in the upper right.

(OH^-) ions. At $T = 10°C$, the equilibrium background charge density of each carrier is 5.21 C/m^3. Thus the measured charge density $q \cong 2$ C/m^3 is a significant fraction of the background charge.

Figure 26 also shows negative charge injection from the negative aluminum electrode of a pair of aluminum electrodes. The velocity v of migrating charges with mobility μ in a field E is $v = \mu E$. Examining Fig. 26 for the cases of positive charge injection from stainless steel electrodes and negative charge injection from aluminum electrodes, we find that the negative charge front has propagated about 35% across the gap in time $t_- = 1.26$ ms in an initial field of $E_- = 115$ kV/cm while the positive charge front has traveled about 71% across the gap in time $t_+ = 1$ ms in an initial field of $E_+ = 130$ kV/cm. The ratio of velocities and fields for the two cases then lets us calculate the ratio of high-voltage charge mobilities

$$\frac{v_-}{v_+} = \frac{0.35/t_-}{0.71/t_+} = 0.40 = \frac{\mu_- E_-}{\mu_+ E_+} = 0.88\frac{\mu_-}{\mu_+} \Rightarrow \frac{\mu_-}{\mu_+} \approx 0.45 \quad (123)$$

to be $(\mu_-/\mu_+) \cong 0.45$. The aluminum measurements were taken at ~5°C. At this temperature the low-voltage hydroxyl ion mobility is about $\mu_- \cong 1.3 \times 10^{-7}$ m^2/V·s. The stainless steel measurements were taken at about 10°C where the low-voltage hydronium mobility is about $\mu_+ \cong 2.9 \times 10^{-7}$ m^2/V·s. The ratio of low-voltage mobilities is then $(\mu_-/\mu_+) \approx 0.45$, in agreement with the measured high-voltage mobilities.

The electroinertial time constant τ_{EI} is then the migration time based on the electrohydrodynamic mobility of Eq. (77)

$$\tau_{EI} = d/(\mu_{EHD}E) = d\sqrt{\rho_d/\epsilon E^2} \quad (124)$$

which at $E = 100$ kV/cm for a 1-cm gap is $\tau_{EI} \approx 1.2$ ms. Because $\mu_{EHD} \approx 8.4 \times 10^{-7}$ m^2/V·s exceeds ion mobilities, it is expected that fluid turbulence might lead to faster charge-migration times. For the unipolar charge injection analysis of Eq. (123) for positive and negative charge carriers, even though the ratio of high-voltage mobilities agrees with low mobility values, the time of flight measurement is faster than that predicted from the low-voltage mobility value. For example, a hydronium ion with mobility $\mu_+ \cong 2.9 \times 10^{-7}$ m^2/V·s in an average field $E \cong 100$ kV/cm would move across a $d = 1$ cm gap in a time $\tau_{mig} \cong d/(\mu_+ E) \sim 3.4$ ms, while the measurements of Fig. 27 show a time of flight ~2 ms. The

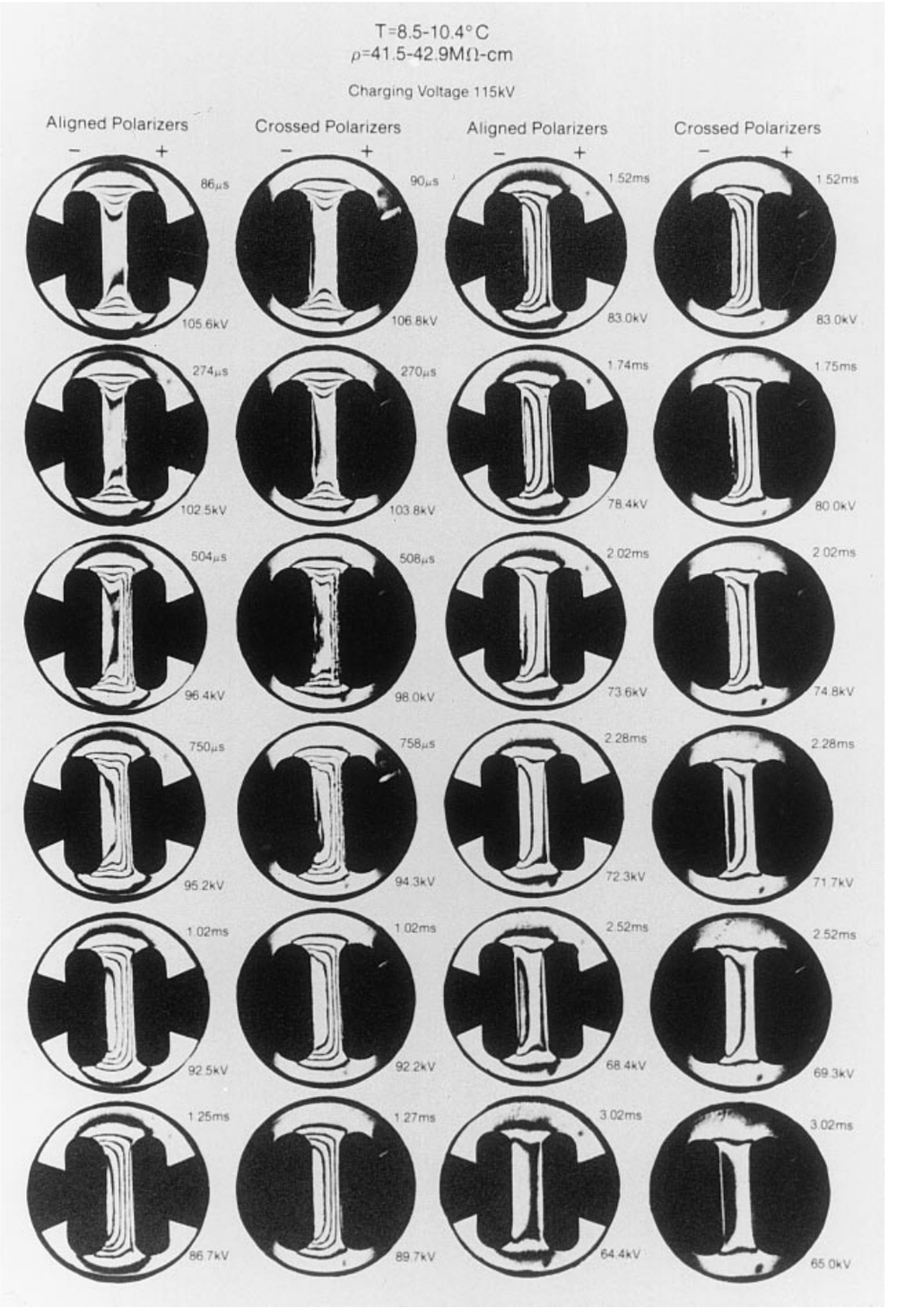

Figure 27. Kerr effect measurements in water using stainless steel electrodes with aligned and crossed polarizers at various times after the start of a high-voltage pulse with initial charging voltage of 115 kV showing positive charge injection (T = 8.5–10.4°C; resistivity 41.5–42.9 MΩ-cm; charging voltage 115 kV).

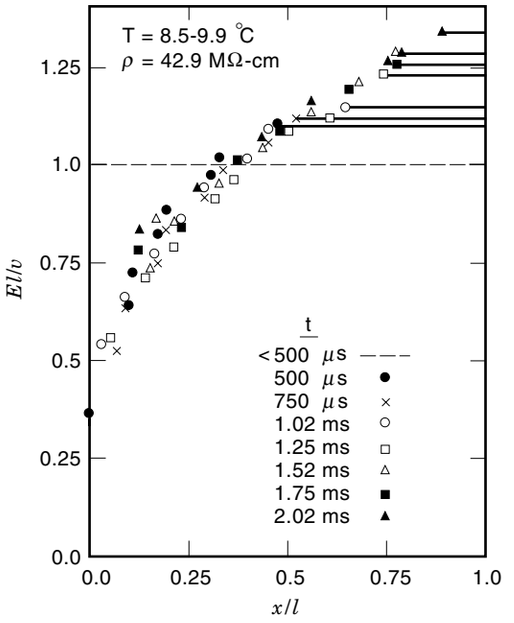

Figure 28. The electric field distribution at various times for the data in Fig. 27 showing field decrease at the positive injecting electrode and field increase at the noninjecting negative electrode at $\bar{x} = x/l = 1$ with a propagating wavefront.

faster time is probably due to fluid motion during the ion transit time causing the enhanced electrohydrodynamic mobility.

Design criteria for high-voltage liquid insulation depend strongly on the electric breakdown strength and typically model the liquid dielectric as a slightly lossy dielectric, simply described by its permittivity and conductivity. For liquid dielectrics there can be significant space-charge injection when high voltage is applied, causing anomalous voltage-current characteristics and distortions in the electric field easily measured using the Kerr electro-optic effect. The sign and magnitude of the space charge depends strongly on the electrode material and voltage polarity. Injected space charge can increase the attainable applied voltage, with the most interesting case being that of bipolar homocharge injection, which decreases the electric fields at both electrodes and for which in small-scale laboratory experiments in highly purified water have allowed up to 40% higher voltage without breakdown.

It is best to inhibit unipolar charge injection that increases the electric field at the noncharge-injecting electrode leading to early electrical breakdown and to encourage bipolar homocharge injection at both electrodes where injected charge shields the electrodes, causing lower electrode fields. Even though this causes the electric field to be larger in the dielectric volume, the intrinsic strength of the dielectric is larger than at interfaces.

SENSITIVE KERR ELECTRO-OPTIC MEASUREMENTS WITH WEAKLY BIREFRINGENT MATERIALS

Measurement of the electric field distributions with low fields or with weakly birefringent materials results in very small light phase shifts. The conventional approach of Eq. (121) with a simple crossed polarizer configuration then has $E \ll E_m$ and the sine may be approximated by its argument, so the light intensity is

$$\frac{I}{I_0} \approx \left(\frac{\pi}{2}\right)^2 \left(\frac{E}{E_m}\right)^4 \tag{125}$$

With $E \ll E_m$, the light intensity in Eq. (125) will be exceedingly small and difficult to detect. A very clever approach to maximize measurement sensitivity for small Kerr constant materials is to apply a voltage to the electrodes which consists of an ac voltage superimposed on a dc voltage (47–51). The frequency of the ac field is chosen to be high enough that space charge behavior will only be influenced by the dc field. The electric field is then described by

$$E = E_0(x, y) + E_1(x, y) \cos \omega t \tag{126}$$

where $E_0(x, y)$ is the dc electric field distribution that satisfies Poisson's equation and $E_1(x, y)$ is the ac electric field that satisfies Laplace's equation. Both dc and ac fields in general can vary with the (x, y) position in the plane perpendicular to the direction z of light propagation.

To further maximize measurement sensitivity, the light phase shift is biased by also inserting a single quarter wave plate between the polarizers as shown in the experimental setup in Fig. 29. Then the transmitted light intensity to the detector is

$$\frac{I}{I_0} \approx \sin^2 \left[\frac{\pi}{2}\left(\frac{E}{E_m}\right)^2 + \frac{\pi}{4}\right] \tag{127}$$

Performing a Taylor's series expansion on Eq. (127), assuming $E \ll E_m$, we obtain

$$\frac{I}{I_0} \approx \left[\frac{1}{2} + \frac{\pi}{2}\frac{E_0^2(x, y)}{E_m^2}\right] + \pi \frac{E_0(x, y)E_1(x, y)}{E_m^2} \cos \omega t + \frac{\pi}{4}\frac{E_1^2(x, y)}{E_m^2} \cos 2\omega t \tag{128}$$

We use a lock-in amplifier to measure the magnitude of the first and second harmonics at position (x, y) which are related to $E_0(x, y)$ and $E_1(x, y)$. The lock-in amplifier allows us to easily extract signals less than 10 μV, very much below the ambient noise level of order 1 mV, by multiplying the input signal with the ac reference signal and low pass filtering it. Such sensitive Kerr measurements have been performed with transformer oil, silicone oil, liquid nitrogen, and melted (≈140°C) low-density polyethylene (LDPE). The Kerr constants for each of these materials were found by integrating the measured electric field distributions between the electrodes and equating the result to the applied voltage. The scaling factor determines E_m and thus B. Note that for arbitrary two-dimensional electrode geometries that the amplitude of the second harmonic optical signal in Eq. (128) is related to the ac electric field amplitude $E_1(x, y)$ which at high enough frequency satisfies Laplace's equation. The fundamental frequency signal in Eq. (128) is proportional to $E_0(x, y)$ which satisfies Poisson's equation. Differences in spatial variations of $E_0(x, y)$ and $E_1(x, y)$ indicate the presence of volume space charge.

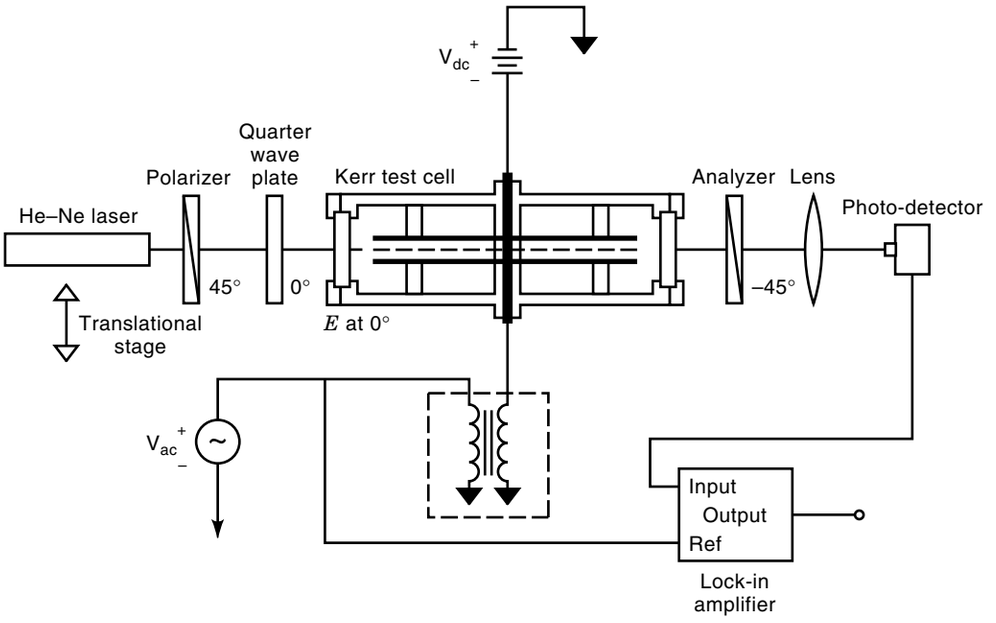

Figure 29. Experimental configuration for sensitive Kerr electro-optic measurements with weakly birefringent dielectrics.

KERR ELECTRO-OPTIC MEASUREMENTS WITH ELECTRIC FIELD MAGNITUDE AND DIRECTION VARYING ALONG THE LIGHT PATH

If the applied electric field direction is constant along the light path, Eq. (119) may be integrated to yield the total phase shift between the components of the light. This total phase shift can be measured by optical polariscopes to noninvasively determine the (transverse) electric field direction φ and magnitude E_T.

Most past experimental work has been limited to cases where the electric field magnitude and direction have been constant along the light path such as two long concentric or parallel cylinders or parallel plate electrodes (42). However, to study charge injection and breakdown phenomena very high electric fields are necessary ($\approx 10^7$ V/m) and for these geometries large electric field magnitudes can be obtained only with very high voltages (typically more than 100 kV). Furthermore, in these geometries the breakdown and charge injection processes occur randomly in space often due to small unavoidable imperfections on otherwise smooth electrodes. The randomness of this surface makes it impossible to localize the charge injection and breakdown and the problem is complicated because the electric field direction also changes along the light path. To create large electric fields for charge injection at known location and at reasonable voltages a point electrode is often used in high voltage research where again the electric field direction changes along the light path. Hence it is of interest to extend Kerr electro-optic measurements to cases where the electric field direction changes along the light path, with specific application for point plane electrodes.

Recent work has presented a new general theory with experimental results of Kerr electro-optic measurements of the electric field whose magnitude and direction changes along the light path, specifically applied to point/plane electrodes (52). The governing differential equations were derived for light propagation in Kerr media and were integrated to predict birefringence patterns for a point/plane electrode geometry with specific parameters used for the high Kerr constant dielectric nitrobenzene ($B \approx 3 \times 10^{-12}$ m/V^2). Characteristic parameters which have been long used in photoelasticity were introduced and in particular extensions of the ac modulation method were developed for cases when the Kerr constant is small (53). Experimental measurements of the characteristic parameters for transformer oil between point/plane electrodes were presented. Utilizing the axisymmetry of the electric field distribution of the point/plane electrode geometry, the experimental characteristic parameter values recovered the electric field using the onion peeling method (54).

ACKNOWLEDGMENTS

Thanks are due to Dr. E. F. Kelley of the U.S. National Institute of Standards and Technology for supplying image converter camera photographs of streamers shown in Figs. 6 and 7. The help of Linda Zahn for making photographic copies of many figures in this article and of Sara Wolfson for preparing the manuscript is also greatly appreciated.

BIBLIOGRAPHY

1. F. M. Clark, *Insulating Materials for Design and Engineering Practice,* New York: Wiley, 1962.
2. R. Bartnikas, *Engineering Dielectrics, Vol. III, Electrical Insulating Liquids,* Philadelphia: ASTM, Monograph 2, 1994.
3. H. G. Erdman, *Electrical Insulating Oils,* Philadelphia: ASTM Special Technical Publication 998, 1992.

4. T. J. Gallagher, *Simple Dielectric Liquids,* Oxford: Clarendon Press, 1975.
5. A. C. M. Wilson, *Insulating Liquids: Their Uses, Manufacture, and Properties,* Stevenage and New York: Peter Peregrinus, Ltd., 1980.
6. T. V. Oommen, C. C. Claiborne, and J. T. Mullen, "Biodegradable Electrical Insulation Fluids," *Proceedings of the Electrical Insulation Conference,* EIC/EMCW, Chicago, IL, Sept. 22–25, 1997, pp. 465–468.
7. J. M. Meek and J. D. Craggs, *Electrical Breakdown of Gases,* New York: Wiley, 1978.
8. R. Bartnikas and E. J. McMahon, *Engineering Dielectrics, Vol. 1, Corona Measurement and Interpretation,* Philadelphia: ASTM Special Technical Publication 669, 1979.
9. A. R. von Hippel, *Molecular Science and Molecular Engineering,* New York, London: Technology Press of MIT and Wiley, 1959.
10. *Annual Book of ASTM Standards;* V. 10.03, *Electrical Insulating Liquids and Gases.* Philadelphia, PA: American Society for Testing and Materials, 1997.
11. R. R. Rogers, IEEE and IEC Codes to Interpret Incipient Faults in Transformers, Using Gas in Oil Analysis, *IEEE Trans. Electr. Insul.* **EI-13**: 349–353, 1978.
12. Special Issue on Flow Electrification in Electric Power Apparatus, *IEEE Trans. Electr. Insul.* **23**: February 1988; S. M. Gasworth, J. R. Melcher, and M. Zahn, Flow-induced charge accumulation in thin insulating tubes, 103–115; N. Kitamura and K. Horii, Behavior of electrostatic charge and velocity distribution of petroleum flowing in relaxation pipe, 117–121; T. V. Oommen, Static electrification properties of transformer oil, 123–128; H. Miyao, M. Higaki, and Y. Kamata, Influence of ac and dc fields on streaming electrification properties of transformer oil, 129–135; D. W. Crofts, The static electrification phenomena in power transformers, 137–146; M. J. Lee, J. K. Nelson, P. S. Shin, and G. Theodossious, Optical studies of electrokinetic processes in dielectric fluids, 147–152; M. Ieda, K. Goto, H. Okubo, T. Miyamoto, H. Tsukioka, and Y. Kohno, Suppression of static electrification of insulating oil for large power transformers, 153–157; D. J. Lyon, J. R. Melcher, and M. Zahn, Couette charger for measurement of equilibrium and energization flow electrification parameters: application to transformer insulation, 159–176.
13. A. Klinkenberg and J. L. Van der Minne, *Electrostatics in the Petroleum Industry.* Amsterdam: Elsevier, 1958.
14. M. Ieda et al., Investigation of static electrification in large power transformers in Japan. In *Proc. Static Electrification in Power Transformers,* EPRI TR-102480, Project 1499-99, June 1993, 2-3-1 to 2-3-31.
15. M. Zahn et al., Dielectric properties of water and water/ethylene glycol mixtures for use in pulsed power system design, *Proc. IEEE,* **74**: 1182–1221, 1986.
16. D. B. Fenneman, Pulsed high voltage dielectric properties of ethylene glycol/water mixtures, *J. Appl. Phys.,* **43** (12): 8961–8968, 1982.
17. I. Adamaczewski, *Ionization, Conductivity and Breakdown in Dielectric Liquids.* London: Taylor and Francis, 1969, 224–225.
18. R. E. Hebner, Measurements of electrical breakdown in liquids. In *The Liquid State and Its Electrical Properties,* E. E. Kunhardt, L. G. Christophoreau, and L. H. Luessen (eds.), New York: Plenum Press, 1988, 519–537.
19. E. O. Forster, Electrical breakdown in liquid hydrocarbons, *J. Electrostatics,* **12**: 1–12, 1982.
20. R. Tobazéon, Streamers in liquids. In *The Liquid State and Its Electrical Properties,* E. E. Kunhardt, L. G. Christophoreau, and L. H. Luessen (eds.), New York: Plenum Press, 465–501, 1988.
21. P. K. Watson, W. G. Chadband, and M. Sadeghzadeh-Araghi, The role of electrostatic and hydrodynamic forces in the negative-point breakdown of liquid dielectrics, *IEEE Trans. Electr. Insul.,* **26**: 543–559, 1991.
22. P. K. Watson and W. G. Chadband, The dynamics of pre-breakdown cavities in viscous silicone fluids in negative point-plane gaps, *IEEE Trans. Electr. Insul.,* **23**: 729–738, 1988.
23. M. Zahn et al., Hydrodynamic shock wave propagation after electrical breakdown, *J. Electrostatics,* **12**: 535–546, 1982.
24. R. E. Hebner et al., Observations of prebreakdown and breakdown phenomena in liquid hydrocarbons, *J. Electrostatics,* **12**: 265–283, 1982.
25. P. P. Wong and E. O. Forster, The dynamics of electrical breakdown in liquid hydrocarbons, *IEEE Trans. Electr. Insul.,* **17**: 203–220, 1982.
26. A. Beroual, C. Marteau, and R. Tobazéon, Behavior of streamers in liquids under step voltage in point-plane geometry, *IEEE Trans. Electr. Insul.,* **23**: 955–959, 1988.
27. J. C. Devins, S. J. Rzad, and R. J. Schwabe, Breakdown and prebreakdown phenomena in liquids, *J. Appl. Phys.,* **52** (7): 4531–4545, 1981.
28. A. Beroual and R. Tobazéon, Prebreakdown phenomena in liquid dielectrics, *IEEE Trans. Electr. Insul.,* **EI-21**: 613–627, 1986.
29. Y. Nakao et al., Effects of additives on prebreakdown phenomena in *n*-hexane, *IEEE Trans. Dielectr. Electr. Insul.,* **1**: 383–390, 1994.
30. D. Linhjell, L. Lundgaard, and G. Berg, "Streamer Propagation under Impulse Voltage in Long Point-Plane Oil Gaps," *IEEE Trans. Dielectr. Electr. Insul.,* **1** (3): 447–458, June 1994.
31. O. Lesaint, "Propagation of positive discharges in long liquid gaps," *Conference Record of the 12th International Conference on Conduction and Breakdown in Dielectric Liquids,* July 15–19, Roma, Italy, 1996, pp. 161–166.
32. R. Badent, K. Kist, and A. J. Schwab, "Prebreakdown Phenomena in Insulating Oil at Large Gap Distances," *Proceedings of the 4th International Conference on Properties and Applications of Dielectric Materials,* July 3–8, 1994, Brisbane, Australia, pp. 103–106.
33. O. Lesaint and G. Massala, "Transition to fast streamers in mineral oil in the presence of insulating solids," *Conference Record of the 1996 IEEE International Symposium on Electrical Insulation,* June 16–19, 1996, Montreal, Quebec, Canada, pp. 733–736.
34. P. Rain and O. Lesaint, "Prebreakdown Phenomena in Mineral Oil Under Step and AC Voltage in Large-gap Divergent Fields," *IEEE Trans. Dielectr. Electr. Insul.,* **1** (4): 692–701, August 1994.
35. M. Zahn et al., Charge migration and transport in high voltage water/glycol capacitors, *J. Appl. Phys.,* **54** (1): 315–325.
36. N. J. Felici, DC conduction in liquid dielectrics (Part II): electrohydrodynamic phenomena, *Direct Current,* **2** (4): 147–165.
37. M. Zahn, "Transient Drift Dominated Conduction In Dielectrics," *IEEE Trans. Electr. Insul.* **EI-12** (2): 176–190, April 1977.
38. M. Zahn, L. L. Antis, and J. Mescua, "Computation Methods for One-Dimensional Bipolar Charge Injection," *IEEE Trans. Ind. Appl.* **24** (3): 411–421, May/June 1988.
39. J. F. Hoburg, "Charge density, electric field, and particle charging in electrostatic precipitation with back ionization," *IEEE Trans. Ind. Appl.* **18** (6): 666–672, Nov./Dec. 1982.
40. M. P. Langevin, "Recombination et Mobilities Des Ions Dans Les Gaz," *Ann. de Chimie et Physique,* **28**: 433–530, 1903.
41. R. E. Hebner, R. A. Malewski, and E. C. Cassidy, "Optical Methods of Electrical Measurements at High Voltage Levels," *Proc. IEEE,* **65** (11): 1524–1548, Nov. 1977.
42. M. Zahn, Space charge effects in dielectric liquids. In *The Liquid State and Its Electrical Properties,* NATO ASI Series B: Physics, Vol. 193, Eds. E. E. Kunhardt, L. G. Christophorou, and L. H. Luessen (eds.), 367–430.

43. E. C. Cassidy et al., Kerr effect studies of an insulating liquid under varied high voltage conditions, *IEEE Trans. Electr. Insul.,* **EI-9**: 43–56, 1974.
44. M. Zahn, Transient drift dominated unipolar conduction between concentric cylinders and spheres, *IEEE Trans. Electr. Insul.,* **EI-11**: 150–157, 1976.
45. M. Zahn and H. Chatelon, Charge injection between concentric cylindrical electrodes, *J. Appl. Phys.,* **48**: 1797–1805, 1977.
46. M. Zahn and T. J. McGuire, Polarity effect measurements using the Kerr electro-optic effect with coaxial cylindrical electrodes, *IEEE Trans. Electr. Insul.,* **EI-15**: 287–293.
47. A. Torne and U. Gafvert, "Measurement of the Electric Field in Transformer Oil Using the Kerr Technique with Optical and Electrical Modulation," *Conference Record of the ICPADM,* IEEE 85CH2115-4, 1985, pp. 61–64.
48. T. Maeno and T. Takada, "Electric Field Measurement in Liquid Dielectrics Using a Combination of AC Voltage Modulation and a Small Retardation Angle," *IEEE Trans. Electr. Insul.,* **EI-22** (4): 503–508, 1987.
49. U. Gafvert et al., "Electric Field Distribution in Transformer Oil," *IEEE Trans. Electr. Insul.,* **EI-27**: 647–660, 1992.
50. T. Maeno, Y. Nonaka, and T. Takada, "Determination of Electric Field Distribution in Oil using the Kerr-Effect Technique After Application of DC Voltage," *IEEE Trans. Electr. Insul.,* **EI-25**: 475–480, 1990.
51. K. Tanaka and T. Takada, "Measurement of the 2-Dimensional Electric Field Vector in Dielectric Liquids," *IEEE Trans. Dielectr. Electr. Insul.,* **1**: 747–753, 1994.
52. A. Ustundag, T. J. Gung, and M. Zahn, "Kerr Electro-Optic Theory and Measurements of Electric Fields with Magnitude and Direction Varying Along the Light Path," *IEEE Trans. Dielectr. Electr. Insul.,* **5**: 421–422, 1998.
53. H. Aben, *Integrated Photoelasticity,* McGraw-Hill International Book Co., New York, 1979.
54. H. K. Aben, "Kerr effect tomography for general axisymmetric field," *Appl. Optics,* **26** (14): 2921–2924, 1987.

MARKUS ZAHN
Massachusetts Institute of Technology